



Originally published as:

Izquierdo-Llavall, E., Menant, A., Aubourg, C., Callot, J., Hoareau, G., Camps, P., Péré, E., Lahfid, A. (2020): Preorogenic Folds and Syn-Orogenic Basement Tilts in an Inverted Hyperextended Margin: The Northern Pyrenees Case Study. - *Tectonics*, 39, 7, e2019TC005719.

<https://doi.org/10.1029/2019TC005719>

# Tectonics

## RESEARCH ARTICLE

10.1029/2019TC005719

### Key Points:

- We propose a new methodological approach to reconstruct fold evolution in hot inverted basins
- Salt-cored folding in the Chainons Béarnais is mostly inherited from extensional stages
- Orogenic shortening in the Northern Pyrenees can be erroneously estimated if this preorogenic, salt-controlled folding is discarded

### Supporting Information:

- Supporting Information S1
- Figure S1
- Figure S2
- Figure S3

### Correspondence to:

E. Izquierdo-Llavall,  
esther.izquierdo-llavall@univ-pau.fr

### Citation:

Izquierdo-Llavall, E., Menant, A., Aubourg, C., Callot, J.-P., Hoareau, G., Camps, P., et al. (2020). Preorogenic folds and syn-orogenic basement tilts in an inverted hyperextended margin: The Northern Pyrenees case study. *Tectonics*, 39, e2019TC005719. <https://doi.org/10.1029/2019TC005719>

Received 15 JUN 2019

Accepted 23 MAR 2020

Accepted article online 27 APR 2020

## Preorogenic Folds and Syn-Orogenic Basement Tilts in an Inverted Hyperextended Margin: The Northern Pyrenees Case Study

Esther Izquierdo-Llavall<sup>1</sup> , Armel Menant<sup>2</sup> , Charles Aubourg<sup>1</sup>, Jean-Paul Callot<sup>1</sup> , Guilhem Hoareau<sup>1</sup>, Pierre Camps<sup>3</sup> , Eve Péré<sup>4</sup>, and Abdeltif Lahfid<sup>5</sup>

<sup>1</sup>Université de Pau et des Pays de l'Adour, E2S UPPA, CNRS, TOTAL, LFCR, Pau, France, <sup>2</sup>GFZ Helmholtz Centre Potsdam, German Research Centre for Geosciences, Potsdam, Germany, <sup>3</sup>Géosciences Montpellier, CNRS et Université de Montpellier, Montpellier, France, <sup>4</sup>CNRS/UNIV PAU and PAYS ADOUR/E2S UPPA, Institut des Sciences Analytiques et de physicochimie pour l'environnement et les matériaux, UMR5254, Pau, France, <sup>5</sup>BRGM, Orléans, France

**Abstract** The Chainons Béarnais (CB, North Pyrenean Zone) resulted from the Cenozoic contractional reactivation of the salt tectonics-bearing, hyperextended margin that initiated at the Europe-Iberia transition during the Early Cretaceous. In this tectonic scenario, assessing the relative contribution of extension and contraction to the present-day structure is crucial to reconstruct the hyperextended margin geometry and to quantify the subsequent shortening. This study undertakes this issue by defining the relationship between folding and two bedding-independent references: peak temperature isotherms and paleomagnetic data. Isotherms were reconstructed from 76 new measurements of Raman spectroscopy on carbonaceous materials (RSCM) and indicate temperatures at the time of peak metamorphism in the CB (110–85 Ma, end of extension). They are shallowly to moderately northwards dipping and cut across most of the folds deforming the Mesozoic units. Paleomagnetic data from 29 sites evidence a widespread remagnetization carried by pyrrhotite that was probably blocked during the early Paleogene (before the onset of continental collision) and postdated folding in the CB. Abnormal inclinations in this remagnetization suggest syn-collision tilts up to 60° to the north in the back limb of the Axial Zone. Based on the presented data set, we propose that the folding of the cover above the evaporitic décollement was almost fully completed by the end of the Cretaceous extension, with ~85–100% of the dip of fold limbs being acquired before the remagnetization time. Cenozoic contraction reactivated the extensional faults in the shallow basement as top-to-the-S thrusts, leading to the passive transport and northwards tilting of the folded cover.

## 1. Introduction

The characterization of fold-and-thrust belts resulting from the inversion of early extensional basins faces one main difficulty: the distinction of inherited, syn-extensional features from those developed during contractional stages. Both contribute to the final geometries of the belt with extensional structures being either preserved, or partly to totally inverted during the contractional event (McClay, 1989). The quantification of their relative contribution is crucial to characterize the early extensional architecture that represents the reference, preorogenic template necessary to estimate the amount of subsequent shortening.

When fold-and-thrust systems involve evaporitic décollements, their geometry significantly differs from that of fold-and-thrust belts dominated by basement faults or detached over a frictional (shale-like) décollement (Callot et al., 2012; Costa & Vendeville, 2002; Coward, 1983; Davis & Engelder, 1985). In general terms, the presence of evaporitic levels enhances (i) out-of-sequence faulting (Letouzey et al., 1995; Santolaria et al., 2015), (ii) quick propagation of contractional deformation towards the foreland (Izquierdo-Llavall et al., 2018; Luján et al., 2003; Pla et al., 2019), and (iii) strong if not complete decoupling between supra-décollement structures and basement features developed underneath (Vendeville et al., 1995). In this scenario, the full understanding of fold-and-thrust systems that reactivate previous extensional basins and involve evaporites requires both (i) the proper distinction between early extensional and later contractional structures and (ii) the proper characterization of cover and basement features and their evolution through time.

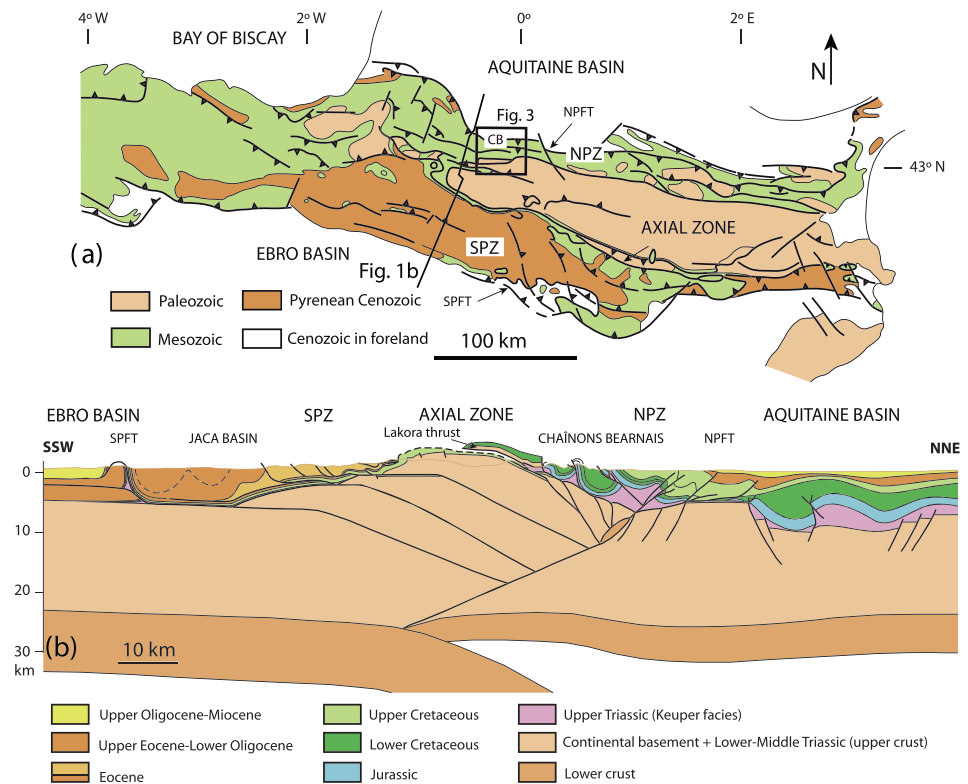


**Figure 1.** a) Geological map of the Pyrenees (modified from Teixell, 1998) with location of the study area (black rectangle). CB, Chaînons Béarnais; NPFT, North Pyrenean frontal thrust; NPZ, North Pyrenean Zone; SPFT, South Pyrenean frontal thrust; SPZ, South Pyrenean Zone. (b) Crustal-scale cross-section across the western Axial Zone (from Teixell et al., 2016). See location in Figure 1a.

Natural examples involving precontractural evaporite units indicate that the relative contribution of syn-contractural and syn-extensional structures in the final deformation pattern may be strongly variable (Graham et al., 2012; Granado et al., 2018). In the Jura Mountains, structural inheritance has been interpreted to be limited to an assemblage of normal faults that offset flat-lying or shallowly dipping beds, the basement and cover units being coupled. These faults then controlled the locus of later contractural thrusts, including the location of the leading edge thrust front (Butler, 1989; Butler et al., 2006). Conversely, in other fold-and-thrust belts such as the Zagros (Callot et al., 2012; Jahani et al., 2007), the Atlas (Calvín et al., 2018; Torres-López et al., 2018), or the eastern Prebetic Zone (Escosa et al., 2018), early diapirs, drape or halokinetic folds, and salt domes accounted for a strong precontractural structuring of the cover units that were partly or largely decoupled from the basement. These early salt structures, weaker than adjacent areas, strongly localized shortening during the subsequent compression that obliterated the precontractural architecture (Callot et al., 2007, 2012; Escosa et al., 2018; Legeay et al., 2019). In this sense, the study of extensional domains affected by mild contractural reactivation (such as the Parentis Basin in the Eastern Bay of Biscay, Ferrer et al., 2008, 2012; Roca et al., 2011) allows a better geometrical and areal characterization of extension-related salt structures.

In the present study, we investigate the precontraction architecture of the Chaînons Béarnais (CB), in the western part of the North Pyrenean Zone (Figures 1 and 2a). The Pyrenees resulted from the inversion during the Late Cretaceous–Miocene of a series of extensional basins formed during a rift-related, high-temperature event that occurred in the Early to mid-Cretaceous (Clerc & Lagabrielle, 2014; Jammes et al., 2009; Lagabrielle et al., 2010; Muñoz, 1992, 2002; Teixell et al., 2016; Tugend et al., 2014). These basins are thought to display a strong preorogenic structuration because of the presence of a thick Triassic salt layer controlling the growth of early detachment anticlines, salt ridges, and diapirs (Canérot, 1989; Canérot et al., 1978, 2005; James & Canérot, 1999; Lagabrielle et al., 2010; Teixell et al., 2016). To further

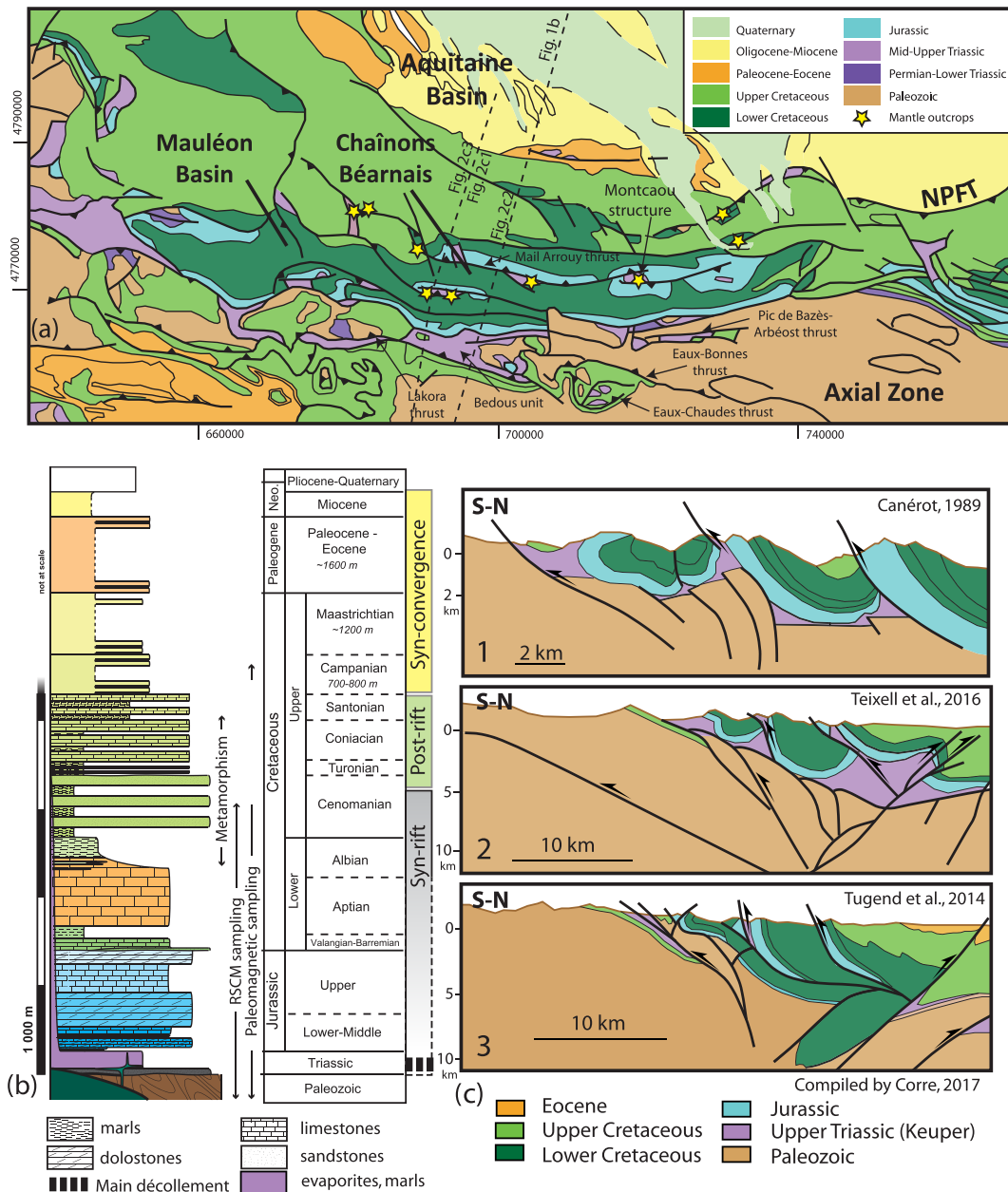


**Figure 2.** (a) Regional geological map of the Chaînons Béarnais area (modified from Barnolas et al., 2008). Yellow stars indicate the location of mantle outcrops (from Lagabrielle et al., 2010). (b) Synthetic stratigraphic log for the Montcaou area. Thickness estimates are given by Casteras et al. (1970) (c) Previously published cross-sections across the study area (Canérot, 1989; Tugend et al., 2014; Teixell et al., 2016; summarized by Corre, 2017, see approximate location in Figure 2a). Note the difference among them in terms of both age and geometry of Triassic-detached structures. The geometry of basement-involved structures and their relationship with the Mesozoic cover also differs in the different sections.

investigate the precontraction architecture in the Northern Pyrenees, we carried out a structural study and constructed two N-S cross-sections through the central part of the CB. Fold geometries along them are semiquantitatively constrained through data derived from two independent methods: Raman spectroscopy on carbonaceous material (RSCM) and paleomagnetism. From these data, we restored preorogenic basin geometries and constrained the relative timing between folding, the freezing of peak-temperature isotherms, and the blocking of the magnetization. Our results indicate that most of the present-day Triassic-cored folds across the studied area developed before the onset of collision in the western Pyrenees, with shortening resulting in the passive transport of the inherited structures and the

tilting of the folded units. The integration of the whole data set puts forward a powerful multimethod approach that can be applied to quantify inheritance in other hot, extensional basins subsequently inverted.

## 2. Geological Setting

The Pyrenean range is the result of the collision between the Iberian and Eurasian plates during Late Cretaceous–Miocene (e.g., Muñoz, 1992). The Pyrenees are bounded by two foreland basins, the Aquitaine basin to the north and the Ebro basin to the south, and they are subdivided into three ESE–WNW-striking structural domains (Figure 1): (i) the North Pyrenean Zone, (ii) the Axial Zone, and (iii) the South Pyrenean Zone that are formed by thick sequences of syn-rift to postrift Mesozoic rocks, Paleozoic sediments and basement rocks, and thick syn-orogenic Cenozoic sequences, respectively. The Pyrenees are a double-verging, asymmetric range, bounded by the North and South Pyrenean frontal thrusts (Figure 1). They consist of a large, south-directed imbricate thrust system associated with a smaller retrovergent belt affecting the northern North Pyrenean Zone (Figure 1b; Muñoz, 1992; Teixell, 1996; Teixell et al., 2016). The present study focuses on the North Pyrenean Zone, north of the western termination of the Axial Zone (i.e., the CB, see location in Figure 1).

### 2.1. Geodynamic Evolution and Stratigraphy of the Northern Pyrenees

The Northern Pyrenees resulted from a long and complex tectonic evolution involving early Mesozoic extensional stages and a late Mesozoic to Cenozoic compression (Teixell et al., 2016 and references therein). These Meso–Cenozoic stages affected a Paleozoic basement previously deformed during the Variscan Orogeny in the Late Carboniferous (Soula et al., 1986; Zwart, 1986).

In the western Axial Zone, the Paleozoic basement mostly consists of Devonian limestones, sandstones, and shales and Carboniferous limestones and turbidites, the latter being coeval to the Variscan deformation stages (García-Sansegundo et al., 2011; Ternet et al., 1980, 2004). During the Variscan Orogeny, these units underwent a syn-orogenic, low-grade metamorphism (anchizone–epizone boundary,  $\sim 300^{\circ}\text{C}$ ; Ternet et al., 2004) and were intruded by late Variscan granitoids (e.g., the Eaux-Chaudes intrusion) that developed limited contact metamorphism around them (Debon, 1996; Ternet et al., 2004). During the Permian–Early Triassic, red detrital units unconformably overlaid Variscan structures. Their deposition took place in extensional to transtensional conditions (Saura & Teixell, 2006; Speksnijder, 1985) and was accompanied by the abundant volcanics that crop out in the central and southern part of the western Axial Zone (Lago et al., 2004; Ternet et al., 2004).

During the Jurassic period, the plate boundary between Iberia and Europe accommodated both extensional and left-lateral strike-slip motions (Canérot, 2008; Jammes et al., 2009, 2010; Rosenbaum et al., 2002; Schettino & Turco, 2011), resulting in a widespread, horst-and-graben-like rifting. Coeval sedimentation was dominated by shallow marine carbonates (Lower Jurassic dolostones and Upper Jurassic platform limestones, Figure 2b) of highly variable thickness across the North Pyrenean Zone, overlying a sequence of evaporites, breccias, and dolerites of Late Triassic age (Canérot et al., 2005; Lagabrielle & Bodinier, 2008).

Extension prevailed during the Early Cretaceous with the development of a complex and localized-in-space rifting that culminated in the formation of a hyperextended margin during the Albian–Cenomanian (Jammes et al., 2009, 2010; Lagabrielle et al., 2010; Masini et al., 2014). At these stages, extreme crustal thinning led to the exhumation of the subcontinental lithospheric mantle along major detachments (Clerc & Lagabrielle, 2014; Jammes et al., 2009; Lagabrielle et al., 2010; Lagabrielle & Bodinier, 2008; Masini et al., 2014). Kinematic models exploring the behavior of the Iberia–Eurasia plate boundary during the Early Cretaceous present discrepancies among them (Barnett-Moore et al., 2016 and references therein). Those compatible with extension in the Pyrenean domain imply an eastwards motion of the Iberian plate relative to Europe that is accommodated by transtension prior to the Late Aptian (Tugend et al., 2015) and during Albian (Nirrengarten et al., 2018). Sedimentation was dominated by platform carbonates during Valanginian–Barremian and upper Aptian. The Valanginian–Barremian sequence is frequently floored by thin layers of red clays containing ferruginous pisolites that evidence partial emersion during the earliest Cretaceous (Ternet et al., 2004). Then, sedimentary environments evolved to deeper, anoxic basins in which volcanic activity was important and deposition of thick sequences of dark marls took place (Debroas, 1987, 1990, Figure 2b). These basins initiated as small half-grabens during the middle Albian,

but subsequently expanded during late Aptian to finally merge into a wider and unique trough during the Cenomanian (Masini et al., 2014; Souquet et al., 1985 and references therein).

Sedimentary units in the North Pyrenean Zone are affected by a high-temperature and low-pressure metamorphism (Golberg & Leyreloup, 1990). This metamorphic event lasted almost 25 Ma between 110 and 85 Ma (late Aptian–Coniacian, Golberg & Maluski, 1988; see review by Clerc et al., 2015). It was characterized by maximum temperatures that ranged between  $\sim 600^{\circ}\text{C}$  and  $<400^{\circ}\text{C}$  (Clerc, 2012; Clerc et al., 2015; Corre, 2017; Ducoux, 2017; Ducoux et al., 2019; Espurt et al., 2019). Peak metamorphism predated the onset of the convergence between the Iberian and European plates whose first evidence in the western North Pyrenean Zone dates of Campanian–Maastrichtian (Poitevin et al., 2014; Teixell, 1996). Early shortening in the Pyrenean domain (Late Cretaceous, 83 to 75–70 Ma, Mouthereau et al., 2014) was first accommodated by the closure of the exhumed mantle domain, followed by continental plate underthrusting (Gómez-Romeu et al., 2019; Jammes et al., 2009; Mouthereau et al., 2014; Teixell et al., 2016; Tugend et al., 2014, 2015). Topography building and foreland flexure were limited during these first convergence stages and could be partly delayed by the presence of a thick salt layer uncoupling the cover from the deep crust and mantle lithosphere (Jourdon et al., 2020). The subsequent full collision stage (from 75–70 Ma to the early Miocene in the Central Pyrenees; Mouthereau et al., 2014; from the late to mid-Eocene in the western Pyrenees; Gómez-Romeu et al., 2019; Teixell et al., 2016) was mostly resolved through the southward thrusting of the upper Iberian crust and the subduction of the lower Iberian crust underneath the European plate (Muñoz, 1992; Teixell, 1998; Teixell et al., 2016). Continental collision was associated with important uplift, foreland flexure, and foreland succession deposition (Biteau et al., 2006; Puigdefàbregas, 1975; Teixell et al., 2016, Figure 1b). In the Northern Pyrenees, syn-orogenic sediments overlaid a postrift sequence made of upper Cenomanian to Santonian carbonated turbidites (Monod et al., 2014, Figure 2b) and consisted of deep-water sediments (Campanian–Maastrichtian) that grade laterally and vertically to shallow marine, transitional (Paleocene–Eocene) and finally continental (Eocene–Miocene) units (Ford et al., 2016; Figure 2b).

## 2.2. Structure of the Northern Pyrenees in the CB Area

The study area encompasses three main structural domains, from south to north, the northwestern Axial Zone, the CB, and the southern Aquitaine basin (Figure 2a). The northwestern Axial Zone consists of Paleozoic rocks, locally overlain by a sedimentary cover of Triassic and Cretaceous units (Figures 2a and 3). Paleozoic units were early deformed during the late Carboniferous (Variscan Orogeny, Matte, 2002) and subsequently affected, during the Pyrenean Orogeny, by several WNW-ESE-striking and south-directed thrusts, forming an imbricate basement thrust system (Figure 1b, Teixell et al., 2016). Among them, the Lákora thrust accommodates a large displacement ( $\sim 17$  km, Teixell, 1996; Teixell et al., 2016, Figure 1b) and has been interpreted to laterally connect to the Eaux-Chaudes and the Eaux-Bonnes basement thrusts across the study area (Teixell, 1996; Tugend et al., 2014; see location in Figure 2a). North of the Axial Zone, the Mesozoic units of the CB are deformed by E-W-trending, tight anticlines that are separated by wider synclines where Albian–Cenomanian marls are preserved (Figures 2a and 3). Mantle rocks crop locally out along the hinge zone of the anticlines that are cut by E-W-striking faults rooted in the Upper Triassic units (e.g., the Mail Arrouy thrust; Casteras, Villanova, & Godechot, 1970; Lacan et al., 2012). The northern boundary of the CB is marked by the North Pyrenean frontal thrust which is characterized by an imbricate fan of north-verging thrusts, poorly emergent to the surface (Biteau et al., 2006; Teixell et al., 2016; Figure 1b). According to Teixell et al. (2016), these thrusts mostly detach along Upper Triassic evaporites in the western CB (Figure 1b), although basement units crop out in the hanging wall of the North Pyrenean frontal thrust across the study area (Figures 2a and 3; Casteras, Canérot, et al., 1970). To the north, a few open folds and thrusts are observed in the Aquitaine foreland basin, extending up to a maximum distance of 50 km to the north of the North Pyrenean frontal thrust (Teixell et al., 2016) and accommodating a limited shortening (Biteau et al., 2006). In addition, seismic lines from the Aquitaine domain evidence the importance of inherited salt-related structures, including frozen reactive diapirs, salt walls, and rollover structures that affected preorogenic Mesozoic sediments (Biteau et al., 2006; Canérot et al., 2005; Espurt et al., 2019; Serrano et al., 2006).

Regarding the folds in the Mesozoic of the CB, various interpretations have been proposed for their timing and geometry at depth (Figure 2c). Previous authors (Fortané et al., 1986; Tugend et al., 2014 and references

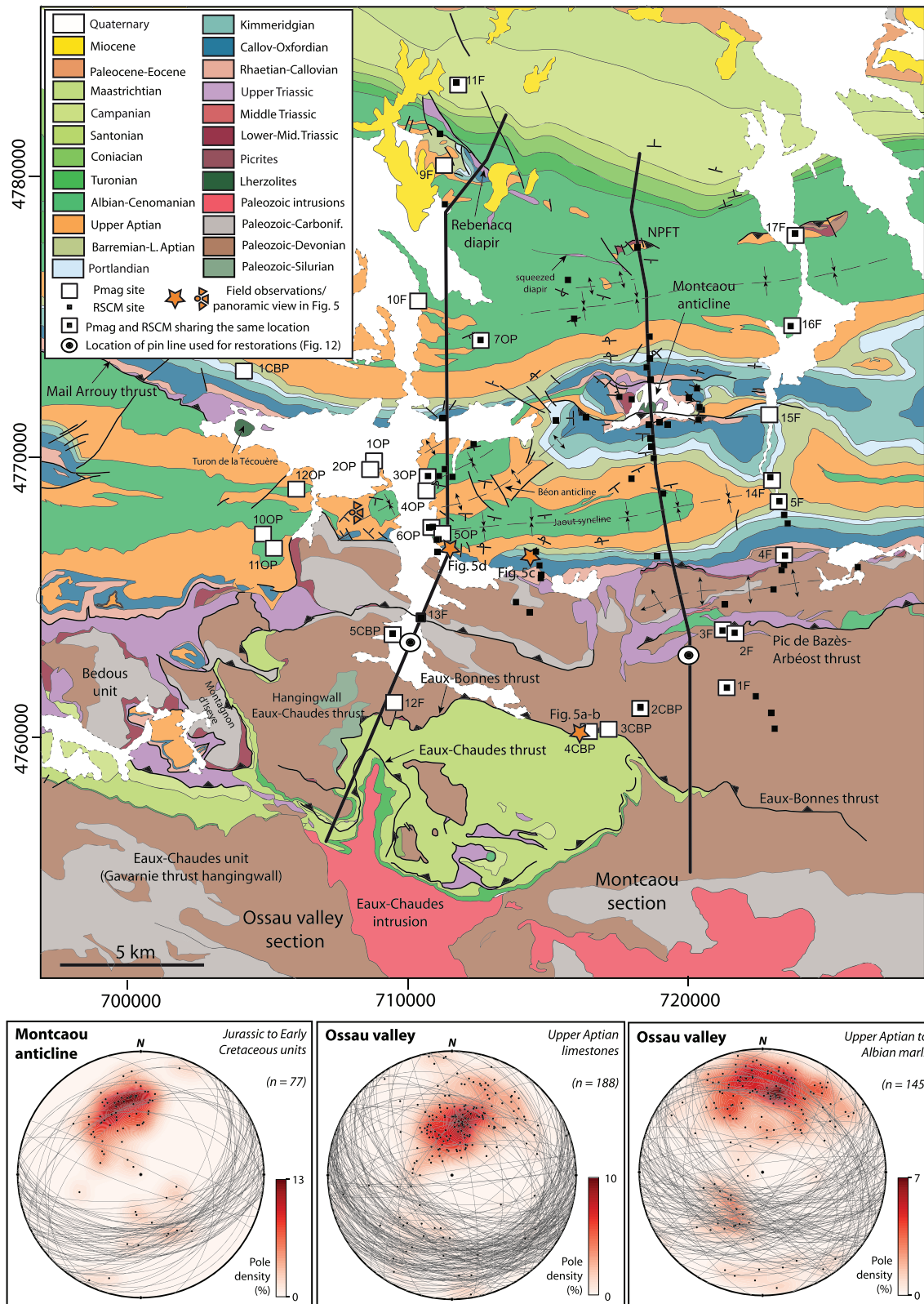


**Figure 3.** Geological map of the study area (modified from Casteras, Canérot, et al., 1970; Casteras, Villanova, et al., 1970; Ternet et al., 1980; Ternet et al., 2004) with location of the sampling sites (paleomagnetism and RSCM) and the cross-sections presented in this work. Bedding measurements along the studied cross-sections (Montcaou cross-section and Ossau valley) are represented in equal-area stereoplots. They indicate a dominant south-dipping bedding, accordingly with the northwards vergence of folds in the Mesozoic. On each stereoplot, the pole density contour is represented and the number of measurements ( $n$ ) is indicated.

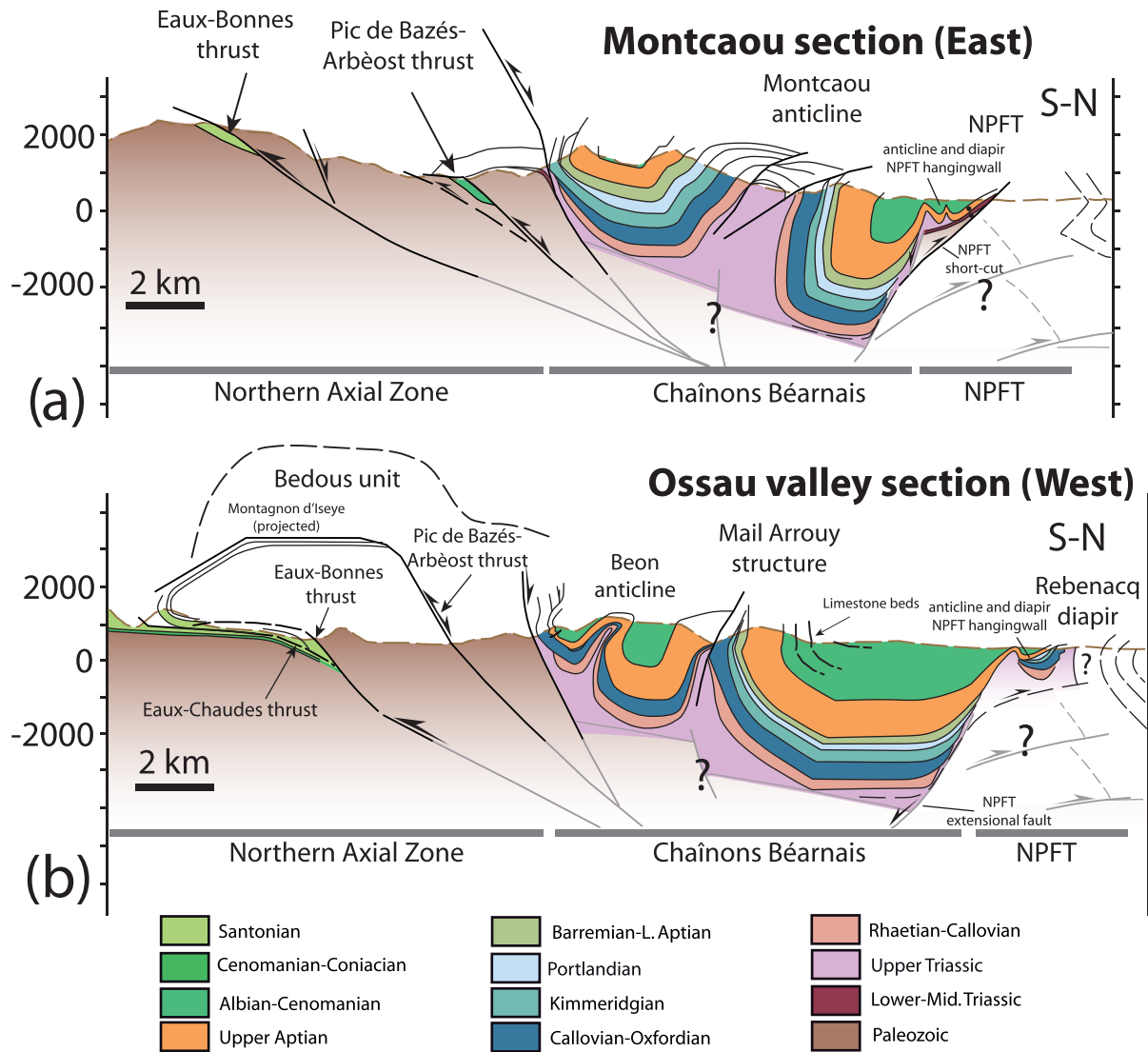


**Figure 4.** Cross-sections across (a) the Montcaou structure and (b) the Ossau valley. See location in Figure 2b.

therein) depicted them as fault-related folds that involve a limited amount of evaporites at depth and developed essentially during contractional stages. Alternative interpretations suggest that they correspond to early detachment folds or diapirs that are cored by moderate (Canérot et al., 2005) or important (Labaume & Teixell, 2014; Teixell et al., 2016) volumes of Upper Triassic evaporites. In this second scenario, folds in the CB have been conceptually interpreted to result from the syn-convergence squeezing of early salt structures formed during the Jurassic and Early to mid-Cretaceous (Canérot et al., 2005; Canérot & Lenoble, 1993; James & Canérot, 1999; Teixell et al., 2016). The driving mechanism and timing of these salt-related structures is also a matter of debate. Lagabrielle et al. (2010) suggested that they resulted from the gravitational gliding of supra-salt sedimentary units towards basin depocenters during the Cretaceous extension, whereas Canérot et al. (2005) proposed that they formed during alternating extensional and compressional stress regimes in the Late Jurassic–Early Cretaceous.

Apart from the geometry and timing of the Triassic-detached structures, previous structural interpretations in the CB (Figure 2c) also disagree on the geometry of the underlying basement structures, mainly due to the lack of available geological and geophysical constraints. Existing studies showed either a moderate degree of coupling between basement and cover structures (Canérot, 1989; Tugend et al., 2014) or a complete decoupling (Corre, 2017; Lagabrielle et al., 2010; Teixell et al., 2016). In the second scenario, previous authors

(Teixell et al., 2016) suggest that the basement underneath the CB is mostly deformed by south-directed thrusts (except the North Pyrenean frontal thrust) and displays a regional, moderate ( $\sim 25^\circ$ ) tilt to the north.

In summary, the comparison of cross-sections derived from previous studies (Figure 2c) emphasizes ongoing debates on the CB about the geometry and timing of Triassic-cored structures and underlying basement-involved thrusts that have to be properly addressed to estimate the relative contribution of extensional and contractional structures to the present-day architecture of the study area.

### 3. From Field and Map Observations to Cross-Section Construction

To better understand the geometry and timing of the structures in the study area, we focused on two representative sections running across the central part of the CB (Figure 3). These cross-sections are based on field observations and newly collected structural data (i.e.,  $\sim 500$  bedding measurements mostly across the Ossau-Montcaou area; Figure 3) as well as on the structural information from existing geological maps (Casteras, Canérot, et al., 1970; Casteras, Villanova, et al., 1970; Ternet et al., 1980, 2004). The cross-sections are separated by a distance of about 9 km from each other with the western one running parallel to the Ossau valley and the eastern one crossing the Montcaou anticline. They extend from the northernmost outcrops of the Axial Zone to the North Pyrenean frontal thrust (Figures 3 and 4).

#### 3.1. Eastern Cross-Section: The Montcaou Section

The northern Axial Zone across the Montcaou section is formed by two main south-directed thrusts, from south to north: the Eaux-Bonnes and the Pic de Bazès-Arbéost thrusts (see location in Figures 3 and 4a). The Eaux-Bonnes thrust superposes Devonian and Carboniferous units onto the Cenomanian to Santonian and Paleozoic sequence of the Eaux-Chaudes unit (Figure 3). Among the latter units, the late syn-rift sequence (Cenomanian) is 25–50 m thick and consists of sandstones and sandy limestones deposited in a tidal environment (Ternet et al., 2004), likely located along the boundary of the Early to mid-Cretaceous Iberian shelf. North-dipping normal faults and shear zones have been recognized in the hanging wall of the Eaux-Bonnes thrust (see Figures 4a, 5a, and 5b), at a short distance from the thrust trace in map view and probably laterally branching to it (see location in Figure 3).

To the north, the Pic de Bazès-Arbéost unit (Figures 3 and 4a) involves Devonian rocks unconformably overlain by Triassic and Albian–Cenomanian units, the Jurassic and lowermost Cretaceous being absent. Here, the Triassic sequence is made of Lower Triassic sandstones and conglomerates overlain by Middle–Upper Triassic shales and carbonates (Muschelkalk and Keuper facies) and abundant dolerites (Ternet et al., 1980). The map view distribution of Triassic rocks in the hanging wall of the Pic de Bazès-Arbéost thrust (Ternet et al., 1980) indicates that this unit is deformed by an E-W-trending basement anticline (Figure 3). The Lower Triassic crops out in the back limb of this anticline and shows a moderate dip to the north ( $\sim 45^\circ$ ; Ternet et al., 1980). Overlying the Triassic or basement units, the Albian–Cenomanian sequence is made of marls and limestones with interbedded breccias and conglomerates (Ternet et al., 1980). From the Eaux-Chaudes to the Pic de Bazès-Arbéost units, the Albian–Cenomanian sequence shows an apparent northward thickening and facies deepening, probably representing a progressive transition to more distal portions of the Early to mid-Cretaceous basin.

To the north of the contact between the Paleozoic basement and the CB, the Mesozoic cover (including a Middle–Upper Jurassic sequence that is absent in the previously described units) is deformed by the Montcaou anticline which is bounded by two synclines. The southern syncline is north verging, and it displays strong stratigraphic thickness variations, especially significant in the Jurassic to Barremian sequence that is thicker in the northern syncline limb (Figures 3 and 4a). The Montcaou anticline is cored by the Keuper units hosting fragments of Lower Triassic rocks and lherzolites (Figure 3). Bedding measurements in this area indicate this fold is north verging: it shows a vertical to overturned northern limb (i.e.,  $90^\circ$  to  $45^\circ$ S), whereas its southern limb dips  $30^\circ$  to  $60^\circ$ S (Figures 3 and 4a). Stratigraphic thickness variations are observed within the sedimentary cover, especially in the Jurassic sequence that thins towards the fold hinge where the base of the Lower Cretaceous limestones represents a folded unconformity (Casteras, Canérot, et al., 1970). Besides, to the west of the section trace, the base of the Albian sequence is also mapped as an angular unconformity overlying Jurassic and older Cretaceous units (Casteras, Canérot, et al., 1970; Figure 3).

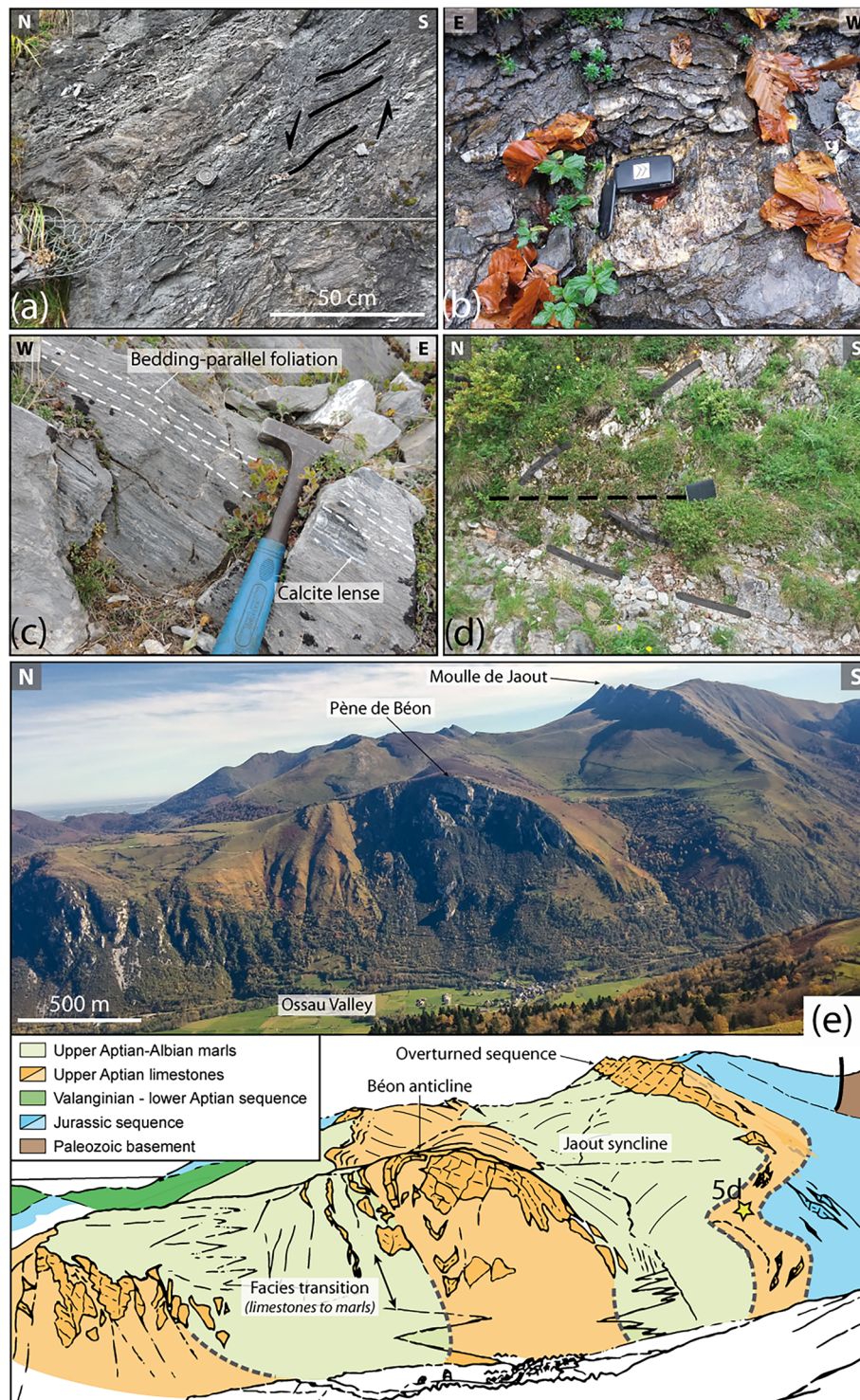


**Figure 5.** Field observations across the studied profiles. See location in Figure 3. (a) Extensional shear bands in the hanging wall of a normal fault affecting Paleozoic units. Eaux-Bonnes unit, Montcaou section ( $x = 716446$ ,  $y = 4760234$ ; UTM coordinates, 30 T, WGS84). (b) Slickenfibres indicating normal faulting sense on the fault zone shown in (a) ( $x = 716416$ ,  $y = 4760190$ ; UTM coordinates, 30 T, WGS84). Eaux-Bonnes unit, Montcaou section. (c) Lower Cretaceous carbonates affected by a penetrative, bedding-parallel foliation in the southernmost outcrops of the CB, Ossau valley cross-section ( $x = 714531$ ,  $y = 4766606$ ; UTM coordinates, 30 T, WGS84). (d) Recumbent fold deforming the Aptian limestones in the southernmost outcrops of the CB, Ossau valley cross-section ( $x = 711305$ ,  $y = 4766923$ ; UTM coordinates, 30 T, WGS84). (e) Interpreted panoramic view of the Bèon anticline and the bounding synclines (see location in Figure 3). Note facies transitions from the hinge of the anticline towards the outer limbs.

To the north of the Montcaou anticline, the trace of the North Pyrenean frontal thrust is marked by two kilometeric-scale outcrops of Paleozoic–Lower Triassic rocks that are directly overlain by a thin sequence of shallowly south-dipping lower Aptian carbonates (i.e., the Upper Triassic, Jurassic, and lowermost Cretaceous sequence is absent). Variations of the stratigraphic sequence and sediment thicknesses between the CB and the hanging wall of the North Pyrenean frontal thrust point out that both domains were separated by an uplifted area that could correspond to a narrow basement high (similar to the Grand Rieu High further west, Teixell et al., 2016), an inflated salt domain, or a combination of both. Paleozoic units were probably brought to the surface (Figures 3 and 4) by an imbricate, north-directed thrust system similar to that depicted further west (Teixell et al., 2016). A detachment anticline with a small wavelength and a squeezed diapir (expressed at surface by a 3.5 km long, narrow strip of Keuper piercing the Cenomanian syn-rift units; labeled as “squeezed diapir” in Figure 3) are recognized in the hanging wall of the North Pyrenean frontal thrust (Figures 3 and 4a), whereas the surface structure in its footwall consists of a north-verging syncline bearing important thicknesses of syn-orogenic units. Paleozoic units underneath this syncline are found by wells at an approximate depth of 4,000–4,500 m below the topographic surface (Serrano et al., 2006).

### 3.2. Western Cross-Section: The Ossau Valley Section

The Ossau valley cross-section is separated from the Montcaou section by less than 10 km, but significant along-strike variations are recognized between them. Regarding the northern Axial Zone, the Eaux-Bonnes thrust splays laterally into two thrust surfaces that superpose Paleozoic and Upper Cretaceous rocks (Cochelin, 2016; Dumont et al., 2015; Izquierdo-Llavall et al., 2012; Ternet et al., 2004) onto the Cenomanian to Santonian rocks of the Eaux-Chaudes unit (see location in Figures 3 and 4b). They are overthrust by the lateral continuation or relay of the Pic de Bazés-Arbèost thrust that juxtaposes on them the Bedous unit, consisting of Paleozoic rocks and thick Triassic, thin Jurassic, and occasional Lower Cretaceous units (Figures 3 and 4b). The whole thrust system draws an antiformal stack geometry with a regional axis plunging to the west. The Bedous unit crops out to the west of the Ossau cross-section, where the Paleozoic and Lower Triassic units forming the Montagnon d'Iseye (see location in Figure 3) likely represent the basement cutoff in the hanging wall of the Pic de Bazés-Arbèost thrust, as projected on the western cross-section (Figure 4b).

The Mesozoic outcrops at the boundary between the northern Axial Zone and the CB are represented by Upper Triassic dolerites and Jurassic–Lower Cretaceous carbonates (Ternet et al., 1980). These units contain intrabedding breccias with calcite-rich matrix and veins within the Callovian–Oxfordian dolomites and the Valanginian limestones. Brecciated facies are partly affected by a penetrative, bedding-parallel foliation with an N-S-trending stretching lineation (Figure 5c). The Jurassic units are unconformably overlain by the Upper Aptian sequence that displays strong thickness variations (Figure 3) and is affected by small-wavelength, recumbent folds (Figures 5d and 5e).

Northward, the Mesozoic cover is deformed by two north-verging anticlines that are laterally connected to the Montcaou anticline (Figure 3) but have a shorter wavelength. The southern anticline (Béon anticline; Figures 3 and 4b) is cored at the surface by Upper Aptian carbonates and has a box fold geometry (Figure 5e). Field observations evidence a facies change from thick limestone beds at the hinge of the anticline that become rapidly thinner towards the outer fold limbs where they laterally grade to marls (Figure 5e). The anticline to the north is largely covered by Quaternary deposits along the Ossau valley and represents the eastward continuation of the Mail-Arrouy thrust (Figure 3). West of the Ossau cross-section, the Mail-Arrouy thrust is NW-SE striking and south verging and juxtaposes north-dipping Triassic and Jurassic units onto subvertical to overturned Albian sequences (Casteras, Villanova, & Godechot, 1970). It involves wide outcrops of Upper Triassic dolerites in its hanging wall (as well as a mantle body, the Turon de la Técoùère, Figure 3), leading us to suggest that Keuper evaporites are still present at depth (Figure 4b). The geometry and vergence of the Mail-Arrouy structure changes across the Ossau valley where it strikes roughly E-W and it is characterized by an overturned, Jurassic–Cretaceous sequence in the northern limb (Casteras, Villanova, & Godechot, 1970). Jurassic units are thinner than in the western part of the structure, and they are locally, unconformably overlain by the Valangian–Barremian sequence (as across the hinge zone of the Montcaou anticline, Figures 3 and 4b).

**Table 1**  
RCSM Temperature Data Obtained Along the Two Transects Across the Montcaou Structure and the Ossau Valley

Sample	Longitude	Latitude	Height (m)	Unit and lithology	Sample type	n spectra	Method	RAI/R2 ratio		Temperature (°C)	
								Mean	SD	Mean	SD
<b>Sites closest to the Montcaou cross-section</b>											
MO16-1	715675	4776281	352	Albian-Cenomanian marls	Thin section	12	L	0.62	0.01	302	7
MO16-1	715675	4776281	352	Albian-Cenomanian marls	Fragment	15	L	0.62	0.01	310	8
A15	723043.35	4760310.47	1439	Lower-Middle Devonian sandstones and shales	Thin section	10	L	0.62	0.01	313	18
A20	721184.14	4763801.52	832	Albian marls	Thin section	13	L	0.63	<0.01	323	9
A14	723780.78	4777937.57	322	Upper Aptian limestones	Thin section	13	L	0.63	0.009	323	12
MO16-15	718153.92	4777424.16	364	Upper Aptian limestones	Thin section	14	L	0.64	<0.01	329	3
MO7-3	716309	4771393	1344	Callovian-Oxfordian dolomites	Fragment	11	B	0.69	0.02	332	7
A18	721340.52	4761768.44	1202	Lower-Middle Devonian sandstones and shales	Thin section	14	B	0.68	0.02	336	9
F 2-9	723612.01	4774639.24	416	Albian-Cenomanian marls	Thin section	13	L	0.64	0.007	336	8
OS9	715894	4774902	387	Albian marls	Fragment	19	L	0.64	0.01	336	14
CBP29	718255.97	4761082.69	1559	Lower-Middle Devonian sandstones and shales	Thin section	13	B	0.68	0.02	337	10
MO4-11	720331	4771306	1034	Lower-Middle Jurassic	Fragment	10	B	0.68	0.01	340	5
MO4-8	720449	4771656	1073	Upper Aptian limestones	Fragment	15	B	0.67	0.02	341	7
MO7-1	715242	4771287	1308	Tithonian dolomites	Fragment	10	B	0.67	0.01	344	4
CBP2	718256.96	4761051.82	1565	Lower-Middle Devonian sandstones and shales	Thin section	11	B	0.66	0.03	346	12
MO2-9	718648.25	4770340.8	1253	Tithonian dolomites	Thin section	19	B	0.66	0.01	346	5
MO5-12	718632	4772720	544	Lower Jurassic	Fragment	10	B	0.66	0.02	346	8
A19	721617.41	4763722.93	956	Lower-Middle Devonian sandstones and shales	Thin section	11	B	0.66	0.02	347	8
MO3-8	719221	4771117	937	Callovian-Oxfordian dolomites	Thin section	17	B	0.66	0.01	347	7
MO2-12	718550.72	4771126	929	Callovian-Oxfordian dolomites	Thin section	13	B	0.66	0.01	347	8
MO6-6	717509	4772120	793	Upper Triassic marls	Fragment	10	B	0.66	0.02	348	10
MO6-5	717945	4772033	716	Permo-Triassic sandstones	Fragment	10	B	0.66	0.01	349	3
A16	722911.97	4760862.09	1384	Lower-Middle Devonian sandstones and shales	Thin section	12	B	0.65	0.01	350	5
MO4-7	720372	4771711	1058	Valanginian limestones	Thin section	25	B	0.65	0.01	350	6
MO4-7	720372	4771711	1058	Valanginian limestones	Fragment	10	B	0.65	0.02	350	9
MO4-3	720277	4772424	1013	Kimmeridgian limestones	Thin section	17	B	0.65	0.02	350	8
MO5-4	718478	4773170	526	Callovian-Oxfordian dolomites	Thin section	17	B	0.65	0.02	350	7
MO5-6	718602.4	4773487.29	695	Tithonian dolomites	Thin section	17	B	0.65	0.02	350	8
MO2-10	718619	4770651	1131	Kimmeridgian limestones	Fragment	20	B	0.65	0.01	351	5
A17	722370.87	4761462.07	1313	Lower-Middle Devonian sandstones and shales	Thin section	11	B	0.64	0.03	354	12
CBP5	709423.96	4763678.57	735	Middle Devonian shales	Thin section	13	B	0.64	0.02	354	9
MO1-5	718951	4771216	813	Lower-Middle Jurassic	Fragment	21	B	0.64	0.01	354	4
OF1	723003.51	4765263.58	590	Lower-Middle Devonian sandstones and shales	Thin section	15	B	0.64	0.02	358	7
F2-8	722887.67	4769261.15	488	Tithonian dolomites	Thin section	11	B	0.63	0.02	359	9
MO2-4	718734	4769937	1436	Lower Aptian marls	Fragment	11	B	0.63	0.01	362	5
MO5-11	718584	4774265	638	Upper Aptian limestones	Thin section	11	B	0.62	0.02	364	7
A22	723290.19	4765952.12	560	Lower-Middle Devonian sandstones and shales	Thin section	13	B	0.62	0.03	366	13
MO3-2	719063	4768680	1258	Albian marls	Thin section	12	B	0.61	0.01	367	6
MO4-6	720367	4771755	1067	Valanginian limestones	Thin section	17	B	0.61	0.01	367	6
MO4-2	719983.35	4772077.5	834	Lower-Middle Jurassic	Thin section	12	B	0.61	0.04	367	17
A21	726006.15	4766059.12	1102	Lower-Middle Devonian sandstones and shales	Thin section	13	B	0.61	0.02	368	11
OF2	723380.56	4766129.41	550	Lower-Middle Devonian sandstones and shales	Thin section	15	B	0.61	0.02	368	10
OF3	723412.6	4766470	544	Lower-Middle Devonian sandstones and shales	Thin section	18	B	0.61	0.04	369	19
F2-5	721267.44	4764730.73	755	Lower-Middle Devonian sandstones and shales	Thin section	10	B	0.6	0.01	376	6
MO2-1	717938	4769208	1523	Upper Aptian limestones	Thin section	19	B	0.58	0.01	383	6

**Table 1**  
Continued

Sample	Longitude	Latitude	Height (m)	Unit and lithology	Sample type	n spectra	Method	RA1/R2 ratio		Temperature (°C)	
								Mean	SD	Mean	SD
MO2-1	717938	4769208	1523	Upper Aptian limestones	Fragment	16	B	0.56	0.01	392	6
5F	723210.03	4768407.01	472	Lower Aptian marls	Thin section	12	B	0.5	0.03	419	13
F2-4	718855.42	4766444.23	1308	Kimmeridgian limestones	Thin section	12	B	0.5	0.03	428	13
F2-7	723384.53	4767918.57	510	Tithonian dolomites	Thin section	10	B	0.38	0.04	470	20
F2-6	723507.79	4767613.75	500	Kimmeridgian limestones	Thin section	11	B	0.35	0.03	483	14
<b>Sites closest to the Ossau valley cross-section</b>											
A2	711284.62	4778974.21	346	Albian marls	Thin section	13	L	<0.55	--	<200	--
A1	711116.26	4781485.96	319	Tithonian dolomites	Thin section	9	L	<0.55	--	<200	--
OS33	711702	4783298	305	Campanian flysch	Fragment	9	L	<0.55	--	<200	--
MO16-06	711231.32	4771375.44	591	Callovian-Oxfordian dolomites	Thin section	18	B	0.68	0.02	339	7
OS10	712555	4774145	397	Albian marls	Fragment	20	L	0.65	0.01	339	11
MO16-5	711184.95	4771357.57	574	Callovian-Oxfordian dolomites	Thin section	16	B	0.66	0.01	346	6
OS32	710685	4769301	766	Albian marls	Fragment	10	B	0.66	0.01	348	5
OS11	712312	4770437	897	Albian marls	Fragment	15	B	0.66	0.01	348	3
OS29	711554	4769274	1032	Albian marls	Thin section	18	B	0.66	0.01	349	5
OS29	711554	4769274	1032	Albian marls	Fragment	17	B	0.6	0.02	374	8
OS30	711280.76	4769547.74	1048	Albian marls	Fragment	10	B	0.65	0.01	351	5
OS31	711076	4769303	972	Albian marls	Thin section	12	B	0.63	0.01	360	4
OS31	711076	4769303	972	Albian marls	Fragment	20	B	0.61	0.03	370	12
MO16-10	711014	4766607	626	Callovian-Oxfordian dolomites	Thin section	10	B	0.6	0.03	375	10
OS2	710857	4767491	691	Albian marls	Fragment	14	B	0.6	0.02	375	9
OS16	710994	4767034	729	Upper Aptian limestones	Thin section	12	B	0.57	0.05	386	22
OS16	710994	4767034	729	Upper Aptian limestones	Fragment	15	B	0.5	0.03	421	15
OS1	710725	4767466	600	Upper Aptian limestones	Thin section	13	B	0.57	0.02	387	11
OS1	710725	4767466	600	Upper Aptian limestones	Fragment	17	B	0.57	0.04	387	18
MO16-28	714531.64	4766606.31	1796	Valanginian limestones	Thin section	12	B	0.56	0.03	390	15
MO16-20	714308.88	4764452.21	1228	Paleozoic shales	Thin section	16	B	0.56	0.04	394	19
MO16-30	713820.53	4764816.12	1517	Paleozoic shales	Thin section	14	B	0.54	0.03	399	12
MO16-24	714723.04	4765782.72	1642	Lower-Middle Jurassic limestones	Thin section	21	B	0.54	0.03	402	13
OS3	711060	4767049	772	Albian marls	Fragment	15	B	0.54	0.03	402	15
MO16-25	714658.66	4766118.67	1756	Callovian-Oxfordian dolomites	Thin section	15	B	0.52	0.04	410	20
MO16-23	714706.12	4765662.76	1604	Lower-Middle Jurassic limestones	Thin section	12	B	0.51	0.03	413	15

Note. For each sample, we provide its location (UTM coordinates, 30 T, WGS84), age and lithology, type (rock fragment or thin section), number of spectra used for calculation of average values ( $n$ ), method used to calculate Raman parameters and temperatures (i.e., L: Lahfid et al., 2010, RA1 ratio; B: Beyssac et al., 2002, R2 ratio). Mean RA1 or R2 ratio and temperature are provided with their corresponding standard deviation (SD). Gray cells indicate sites where measurements were carried out on both rock fragments and thin sections (see Figure S1 in Supporting Information).

North of the Mail-Arrouy structure, a wide syncline crops out (wider than across the Montcaou section), characterized by a 5 km long, flat-lying hinge zone. The North Pyrenean frontal thrust across the Ossau section is represented by the NW-SE-elongated Rebenacq diapir (see location in Figure 3). This structure consists of Keuper evaporites partly overlain by a thin Jurassic and Lower Cretaceous sequence (Figures 3 and 4b). In the western cross-section, and similarly to the Montcaou cross-section, the Rebenacq diapir is interpreted to be northwards transported in the hanging wall of a north-directed thrust that (conversely to the Montcaou section) is not involving Paleozoic units at surface in its hanging wall.

## 4. Peak Temperatures Study

### 4.1. Methodology

An RSCM study was carried out to assess peak temperatures across the two presented cross-sections. Seventy-six samples (Table 1, Figure 3) were collected from fresh outcrops, distributed throughout all fold limbs and thrust units, both in the North Pyrenean and Axial Zones. Samples were collected across the different stratigraphic units cropping out and encompass the whole prerift and syn-rift cover sequence plus the Paleozoic basement units (Table 1; Figure 2).

The RSCM technique provides a good estimate of a wide range of peak temperatures (200–650°C) in sedimentary rocks (Beysac et al., 2002; Lahfid et al., 2010). RSCM analyses were carried out at the Bureau de Recherches Géologiques et Minières (BRGM, Orléans, France) and Institut des sciences analytiques et de physico-chimie pour l'environnement et les matériaux (IPREM, Pau, France) laboratories. Measurements at the BRGM were acquired by means of a Renishaw inVia Reflex system with argon-ion laser. The laser beam (514-nm wavelength) was focused on the sample with power of around 0.5 mW at the thin section surface, through a Leica DM2500 microscope specially adapted for the system using a  $\times 100$  magnification objective. A similar approach was applied on a Spectra-Physics system (model Stabilite 2018) at IPREM. The laser beam was focused through an Olympus BX40 microscope, and a maximum power of 1 mW during 45 and 60 s was used. Raman spectra from carbonaceous particles were recorded until obtaining at least 10 consistent spectra ( $n$  in Table 1). Spectra indicating higher, out-of-range temperatures were identified as possible anomalies related to older thermal events (i.e., thermal inheritance) and discarded for the average temperature calculations.

We analyzed a total of 51 thin sections and 25 rock fragments (Table 1). Thin sections were polished, and to avoid the effect of polishing on the structural state of carbonaceous material, measurements were carried out on particles located below transparent minerals, usually calcite or quartz. Rock fragments provide a fast acquisition of Raman spectra in organic-rich lithologies, especially in the Albian marls, where measurements were performed on fresh cuts to limit the alteration of organic material. To check the consistency between the two approaches, both rock fragment and thin section measurements were performed on seven “calibration” sites (highlighted in gray in Table 1). Results from these comparative tests show consistent mean peak temperatures (similar to Aoya et al., 2010) and corresponding standard deviations for 6 out of 7 samples, with mean values from fragments being usually slightly higher, independently from the lithology and the temperature range (Table 1, Figure S1 in Supporting Information). Typically, reliable spectra were obtained in the Albian and Paleozoic shales and marls and dark Jurassic carbonates, whereas the recognition of appropriate carbonaceous particles was more difficult in the Aptian and Paleozoic, carbonate-rich units (measurements on rock fragments from these units were discarded). Temperature values from spectra analysis were calculated with Peakfit Software (Systat), following the protocol and calibration proposed by Beysac et al. (2002) for the higher temperatures (i.e., 330–650°C, B method in Table 1) and extended to the 200–320°C range by Lahfid et al. (2010; L method in Table 1).

### 4.2. Results: Distribution of Peak Temperatures

Peak temperatures range between values  $<200^\circ\text{C}$  up to  $483 \pm 14^\circ\text{C}$ , according to Lahfid et al. (2010) and Beysac et al. (2002) calibrations, respectively (Table 1; Figure 6). Standard deviations of site mean temperatures range from  $3^\circ\text{C}$  to  $22^\circ\text{C}$ . They are  $<10^\circ\text{C}$  in 65% of the sites and generally lower than the uncertainty inherent to the RSCM calibration (temperature errors in the reference data used for calibration range between  $15^\circ\text{C}$  and  $50^\circ\text{C}$  with an average of  $\sim 30^\circ\text{C}$ , Beysac et al., 2002).

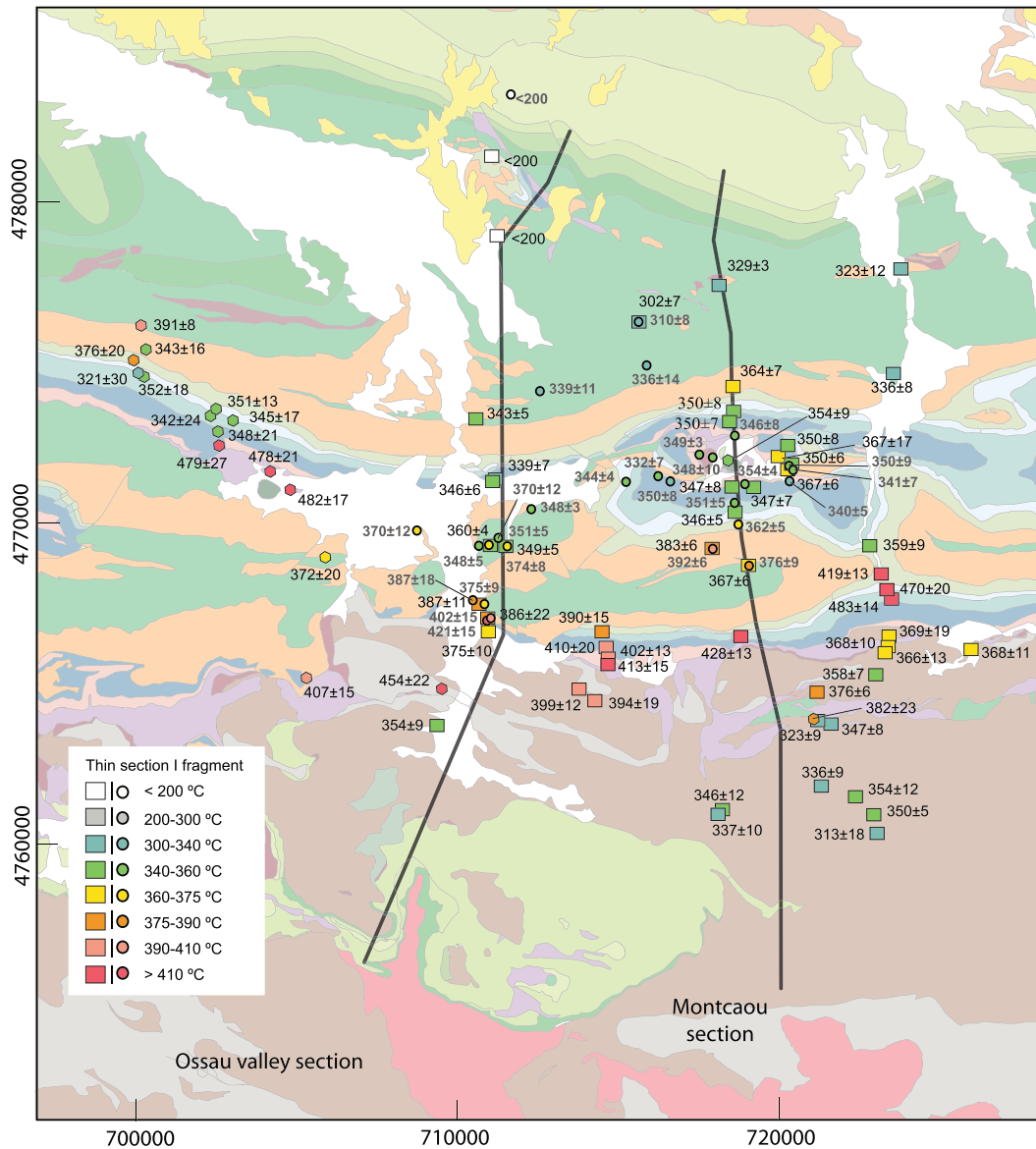


**Figure 6.** Peak temperatures estimates obtained from RSCM. Mean temperature values (and standard deviations) from this and previous studies (Clerc, 2012; Corre, 2017) are indicated. Circles and gray values represent rock fragments, whereas squared symbols and black values indicate thin sections. Hexagonal symbols refer to temperature estimates from the previous studies, obtained in all cases from thin section samples.

When temperature data are grouped by stratigraphic units, no significant differences are found between the Paleozoic basement ( $358 \pm 21^\circ\text{C}$ ), the Triassic–Jurassic ( $369 \pm 41^\circ\text{C}$ ), and the Cretaceous ( $360 \pm 29^\circ\text{C}$ ) cover units (see Figure S2 in Supporting Information). This distribution evidences that no direct relationship exists between peak temperatures and the stratigraphic position of the units.

Considering the structural units, temperatures are generally higher in the northern Axial Zone and the southern CB and decrease progressively both to the north and to the south (Figure 6). Across the Axial Zone, we determined a temperature shift from  $\sim 320\text{--}350^\circ\text{C}$  in the hanging-wall of the Eaux-Bonnes thrust to  $\sim 370\text{--}400^\circ\text{C}$  in the hanging-wall of the Pic de Bazès-Arbéost thrust (Figure 6; see location in Figure 3). Temperatures in the northern Axial Zone are very similar to those obtained in the southernmost outcrops of the CB across the Ossau valley section ( $\sim 375\text{--}420^\circ\text{C}$ ), but considerably lower than those recorded in the Jurassic units that crop out along the Montcaou section ( $\sim 430\text{--}480^\circ\text{C}$ ; Figure 6). Temperature values in the CB decrease to the north, displaying an almost homogeneous temperature of  $\sim 340\text{--}360^\circ\text{C}$  across the

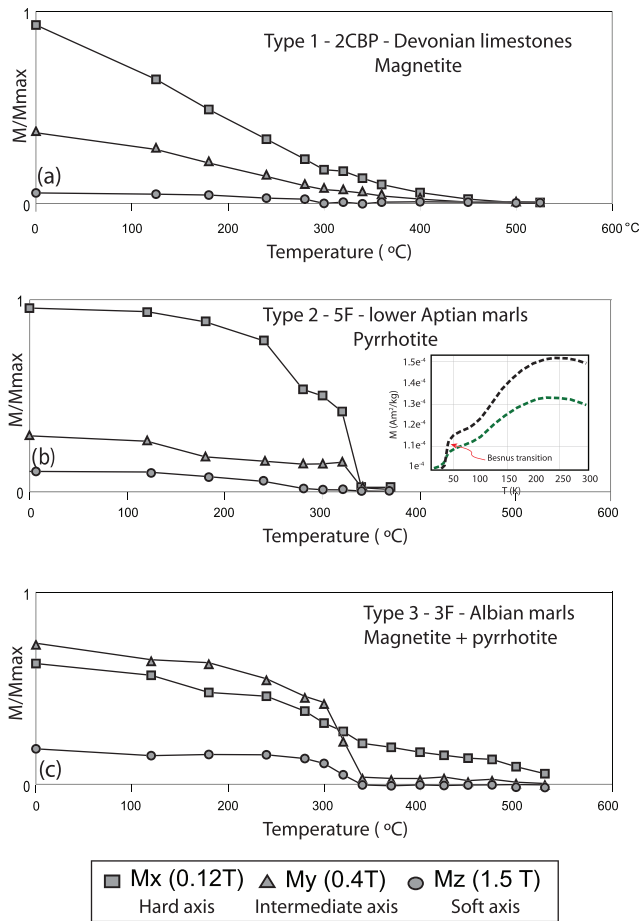


**Figure 7.** Stepwise thermal demagnetization of the composite IRM (Lowrie, 1990) for representative samples of type 1, type 2, and type 3 curves (see explanation in the text). Applied fields are 1.5, 0.4, and 0.12 T. The low-temperature magnetization experiment in Figure 7b was carried out in a sample from RSCM site OS11 (see location in Table 1). The peak temperature in this site is  $348 \pm 3^\circ\text{C}$ .

magnetizer was used to apply three different, decreasing magnetic fields of 1.5, 0.4, and 0.12 T along the three mutually perpendicular axes of the standard specimens. Besides, temperature-dependent magnetization experiments at low temperature (in the range 10–300 K) were also carried out.

## 5.2. Results

### 5.2.1. Magnetic Mineralogy

Three different types of curves can be differentiated, according to the thermal demagnetization of the composite IRM (Figure 7):

1. The type 1 curves display a negligible magnetization along the hard axis (1.5 T) and a hyperbolic decay of the intermediate and/or soft axis (0.4 and 0.12 T) from room temperature up to  $450\text{--}550^\circ\text{C}$  (Figure 7a). This range of unblocking temperatures ( $T_{ub} < 550^\circ\text{C}$ ) and the soft coercivity indicates that magnetite (potentially altered to maghemite) is the main magnetic carrier (Lowrie, 1990). We observed type 1 curves in samples from sites located in the Paleozoic of the Eaux-Bonnes unit and the lower Aptian marls in the hanging wall of the North Pyrenean frontal thrust (site 9F, Figure 3). Note that peak temperatures are generally  $<340^\circ\text{C}$  in the area where these samples are located (Figure 6; Table 2).
2. The type 2 curves are characterized by a magnetization which resides in the intermediate (0.4 T) and soft axis (0.12 T) and unblocks at  $T_{ub} < 340^\circ\text{C}$  (Figure 7b) which suggests that the magnetic carrier is an iron sulphide (Lowrie, 1990). We identified this behavior in samples from the lower Aptian marls (Figure 7b) of the CB and the Paleozoic (12F and 4F), where peak temperatures are  $>350^\circ\text{C}$ .

Montcaou anticline and its lateral continuation to the west. Lower values are measured northward, in the hanging wall of the North Pyrenean frontal thrust, with average temperatures of  $300\text{--}330^\circ\text{C}$  to the east (i.e., thrust involving basement units, Figure 4a) and  $<200^\circ\text{C}$  to the west (i.e., Rebenacq diapir, Figure 4b).

## 5. Paleomagnetic Study

### 5.1. Methodology

Peak temperature estimates were completed with 29 new paleomagnetic sites (254 demagnetized cores) along the Mesozoic and Paleozoic units cropping out in the studied profiles. Fine-grained, phyllosilicate-rich units were preferably chosen. Mesozoic sites were mostly collected across the syn-rift, Albian shales (13 sites) although Aptian limestones (two sites), shales (three sites) and basalts (one site), and Jurassic limestones (two sites) were locally sampled. Paleozoic sites (eight sites) include Devonian and Carboniferous limestones and slates. We collected at least one site per fold limb across the kilometeric wavelength folds deforming the CB and the North Pyrenean frontal thrust domain.

Magnetization was measured with both Agico Spinner (Géosciences Environnement Toulouse [GET]) and 2D squid magnetometers (Universities of Burgos and Montpellier), whereas stepwise thermal demagnetization was operated with shielded furnaces, at temperature steps ranging from  $20^\circ\text{C}$  to  $100^\circ\text{C}$  and up to a maximum temperature of  $560^\circ\text{C}$ . We determined the paleomagnetic components by means of principal component analysis (PCA), averaged the directions obtained by sites, and computed the statistical parameters assuming a Fisherian distribution (Fisher, 1953) with the routine supplied by Remasoft (Chadima & Hrouda, 2006). The statistical confidence of fold tests was determined through the online module provided by Paleomagnetism.org (Koymans et al., 2016), based on Tauxe and Watson (1994) method.

To determine the carriers of the magnetization, we conducted thermal demagnetizations of the composite isothermal remanent magnetization (IRM, Lowrie test, Lowrie, 1990) on 15 representative samples. A 2G pulse

**Table 2**  
*Location of Paleomagnetism Sites with Indication of the Sampled Unit, the Main Magnetization Carrier, and the NRM Intensities*

Site name	X coordinates	Y coordinates	Unit and lithology	Magnetic carrier	Mean NRM Intensity (mA/m)	Closest RSCM peak temperature (°C, site)
1OP	708760	4769763	Albian shales	Pyrrhotite	0.30	370 ± 12 (1OP)
2OP	708639	4769558	Albian shales	Pyrrhotite	0.07	370 ± 12 (1OP)
3OP	710685	4769301	Albian shales	Pyrrhotite	0.90	348 ± 5 (OS32)
4OP	710633	4768803	Albian shales	Pyrrhotite	1.51	348 ± 5 (OS32)
5OP	711206	4767299	Albian shales	Pyrrhotite	8.03	402 ± 15 (OS3)
6OP	710845	4767495	Albian shales	Pyrrhotite	9.35	375 ± 9 (OS2)
7OP	712555	4774145	Albian shales	Pyrrhotite	0.73	339 ± 11 (OS10)
10OP	704784	4767243	Albian shales	Pyrrhotite	--	407 ± 15 (Corre, 2017)
11OP	705206	4766762	Albian shales	Pyrrhotite	--	407 ± 15 (Corre, 2017)
12OP	706004	4768854	Albian shales	Pyrrhotite	--	372 ± 20 (Corre, 2017)
1CBP	704158	4773029	Kimmeridgian limestones	Magnetite	3.86	345 ± 17 (Corre, 2017)
2CBP	718256.96	4761051.82	Lower Devonian limestones	Pyrrhotite	0.15	346 ± 12 (CBP2)
3CBP	717125.05	4760274.81	Lower Devonian limestones	Pyrrhotite	11.05	346 ± 12 (CBP2)
4CBP	716446.37	4760222.43	Lower Devonian limestones	Magnetite + Pyrrhotite	0.11	346 ± 12 (CBP2)
5CBP	709423	4763678	Lower–Middle Devonian shales	Magnetite + Pyrrhotite	0.14	354 ± 9 (CBP5)
1F	721340.57	4761768.44	Lower Devonian limestones	Magnetite	0.45	336 ± 9 (A18)
2F	721617.42	4763722.92	Lower Devonian limestones	Pyrrhotite	0.39	347 ± 8 (A19)
3F	721205.82	4763833.13	Albian shales	Pyrrhotite	0.38	323 ± 9 (A20)
4F	723386.68	4766467.19	Lower Devonian limestones and shales	Pyrrhotite	0.28	369 ± 19 (OF3)
5F	723210.03	4768407.01	Lower Aptian shales	Pyrrhotite	110.27	419 ± 13 (5F)
9F	711263.65	4780378.87	Lower Aptian shales + volcanics	Magnetite	3.74 (marls) 7.54 (volcanics)	< 200 (A1)
10F	710349.55	4775564.33	Upper Aptian limestones (Urgonian limestones)	Magnetite	0.04	---
11F	711761.66	4783266.15	Campanian turbidites	Magnetite	0.38	< 200 (OS33)
12F	709498.49	4761241.56	Lower Devonian limestones	Magnetite + Pyrrhotite	0.80	---
13F	710405.09	4764202.77	Lower Carboniferous shales and limestones	Magnetite	0.005	---
14F	723006.84	4769079.78	Lower Aptian shales	Pyrrhotite	0.16	359 ± 9 (F2-8)
15F	722859.42	4771514.68	Portlandian limestones	---	0.40	---
16F	723661.05	4774690.93	Albian shales	Magnetite	0.32	336 ± 8 (F2-9)
17F	723804.4	4777907.46	Upper Aptian limestones (Urgonian limestones)	---	0.05	323 ± 12 (A14)

Note. RSCM temperatures from sites located at a distance lower than 2 km are indicated.

3. The type 3 curves are characterized by a strong decay of the hard and/or intermediate axis (1.5 and 0.4 T) at ~340°C and a hyperbolic decay along the intermediate and/or soft axis (0.4 and 0.12 T) from room temperature up to 550°C (Figure 7c). This behavior suggests a mixture of medium- to hard-coercivity minerals with  $T_{ub} < 340^\circ\text{C}$  (iron sulphides) and soft-coercivity minerals with  $T_{ub} < 550^\circ\text{C}$  (magnetite, Lowrie, 1990). Type 3 curves were measured in samples from the Kimmeridgian limestones in the hanging wall of the Mail Arrouy thrust (1CBP), the Albian marls unconformably overlying the Paleozoic in the hanging wall of the Pic de Bazès-Arbéost thrust (3F, Figure 7c), and the Paleozoic in the Ossau valley (13F).

Magnetite and iron sulphides in the North Pyrenean Zone were previously described by Oliva-Urcia et al. (2010) in the Mauléon Basin (to the west of our study area, see location in Figure 2). To better precise the iron sulphide types present in the CB, we ran low-temperature magnetization experiments in samples collected along the Albian marls, following the protocol proposed by Aubourg and Pozzi (2010). The saturated isothermal remanent magnetization acquired at 300 K (RT-SIRM) shows a large drop on cooling at ~35 K (Figure 7b). On warming, the recovery of RT-SIRM is not reversible. These observations define the Besnus magnetic transition (Dekkers et al., 1989; Rochette et al., 1990) which is characteristic of monoclinic pyrrhotite ( $\text{Fe}_7\text{S}_8$ ).

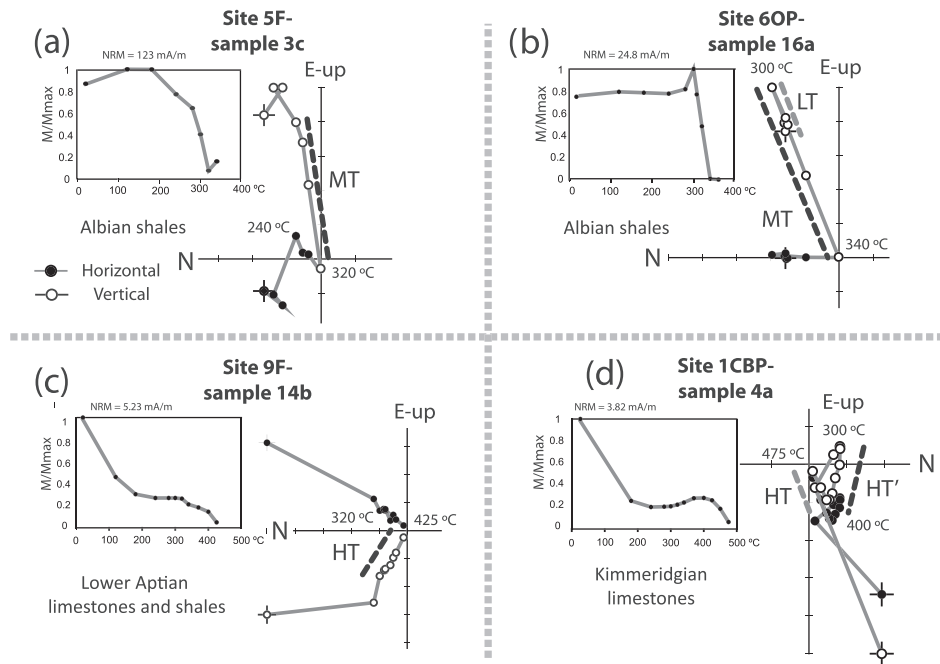


**Figure 8.** Paleomagnetic results from the stepwise thermal demagnetizations in orthogonal plots. Diagrams from the different recognized components and sampled units are represented (geographic coordinates). The magnetic intensity decay during stepwise demagnetization is also shown. In the orthogonal diagrams, black (white) circles are projected on the horizontal (vertical) plane.

### 5.2.2. Paleomagnetic Components: Unblocking Temperatures and Polarities

Natural remanent magnetization (NRM) varies over five orders in magnitude ( $10^{-3}$ – $10^2$  mA/m, Table 2). In some samples (but never systematically at the site scale), we observed a rather weak viscous overprint for  $T_{ub} < 240^\circ\text{C}$ , parallel to the present-day magnetic field. Stepwise thermal demagnetization reveals the presence of a complex magnetization consisting of three components that are distinguishable by their unblocking temperature range: a lower (LT,  $280$ – $300^\circ\text{C}$ ), an intermediate (MT,  $300$ – $340^\circ\text{C}$ ), and a high-temperature component (HT,  $320^\circ\text{C}$  up to  $530^\circ\text{C}$ ).

LT and MT components, both carried by pyrrhotite, were found in 78% of the sites where stable paleomagnetic components could be defined. The most widespread component is the MT one (18 sites) that is generally a characteristic remanent magnetization (ChRM), stable through thermal demagnetization (Figures 8a and 8b). In geographic coordinates, polarities of MT component are reversed (eight sites), normal (four sites), and dual (three sites). In six sites, MT components coexist with the LT component. LT components display polarities that are systematically the opposite to those of the MT components (Figure 8b) and have been detected in the Albian marls along the Ossau valley and in a Paleozoic site (12F; Table 3).

The HT component, carried by magnetite, shows a site-scale dispersion that is generally higher than in LT and MT components (see Table 3). It displays both normal and reverse polarities in geographic coordinates and commonly represents the single component at the site scale (Figure 8c).

### 5.2.3. Fold Test and Comparison to the Reference Direction

When possible, we carried out fold tests across the target structures (i.e., the folds affecting the CB) where component MT was used. Fold test results (summarized in Figures 9a to 9c) indicate that MT groups better in geographic coordinates, being post- to late syn-folding in the Béon anticline and the two related synclines in the Ossau cross-section (better grouping after  $<17\%$  unfolding, Figures 9a to 9c). At the unfolding step showing the best clustering (0–17%), MT is mostly north directed and displays a steep, upward plunge. Fold tests in the lateral continuation of the Jaout syncline across the Montcaou section (sites 5F and 14F, see location in Figure 3) and the Mail Arrouy structure (sites 3OP and 7OP) show two best fit maxima at 0 and 100% of unfolding that are not statistically distinguishable from each other. Nevertheless, considering (i) fold test results in the southern Ossau cross-section (Figures 9a to 9c), (ii) the tight clustering of MT

**Table 3**  
Summary of Paleomagnetic Directional Data

Site	Comp.	$n/N$	D (BTC)	I (BTC)	$\alpha_{95}$	$k$	Bedding	D (ATC)	I (ATC)	Polarity
12F	LT	4/8	201	-57	9	111	012,60	197	3	Geo 3R/1N
	MT	8/8	6.5	60	4	216	012,60	9	0	Geo 6N/2R
	HT	3/8	357	60	10	165	012,60	4.5	1	Geo 2N/1R
5CBP	HT	7/14	131	-19	10	40	015,83	129	21	Geo 5N/2R
	MT	4/14	335	45	21	20	015,83	344	-27	Geo N
13F	HT	4/8	59	45	34	8	346,82; 243,71	29	-6	Geo N
2CBP	MT	5/9	173	-71	14	30	055,70	218	-11	Geo 2N/3R
1F	HT	3/8	189	-37	13	95	151,49	246	-61	Geo R
2F	MT	7/11	95	72	10	37	033,77	49	4	Geo N
3F	MT	4/10	339	68	29	11	037,62	18	15	Geo N
4F	MT	4/11	257	-53	32	10	315,43	193	-54	Geo R
1OP	MT	11/14	241	-68	8	36	109,20	262	-52	Geo R
	LT	6/14	35	84	23	10	109,20	94	68	Geo N
2OP	MT	7/14	237	-52	9	47	227,18	244	-70	Geo R
	LT	8/14	48	54	12	21	227,18	48	72	Geo N
3OP	MT	10/12	177	83	12	18	174,72	174	11	Geo N
	LT	11/12	293	-75	6	58	174,72	341	-11	Geo R
4OP	MT	9/13	352	-53	4	158	35,146	242	25	Geo R
5OP	MT	13/14	26	-65	3	287	43,119	230	5	Geo R
	LT	13/14	200	65	4	138	43,119	52.5	-6	Geo N
6OP	MT	13/15	11	-73	4	139	197,69	15	-3	Geo R
	LT	10/15	203	74	8	37	197,69	199	5	Geo N
7OP	MT	6/14	267	-66	13	28	336,124	180	23	Geo R
10OP	MT	5	16	-64	17	29	176,21	8	-44	Geo R
11OP	MT	7	194	-46	4	228	038,21	202	-26	Geo R
12OP	MT	6	122	-65	6	118.5	135,24	165	-86	Geo R
1CBP	HT*	10/11	118	-68	5	91	042,51	193.5	-41	Geo R
	HT	10/11	249	43	6	74	042,51	329	69	Tilt N
9F	HT	14/16	10	35	4	110	140,28	33	49	Tilt N
5F	MT	6/8	92	-81	25	8	12,121	182	29	Geo R
14F	MT	5/9	175	79	6	175	165,50	167	29	Geo 4N/1R
16F	HT	4/17	149	-56	17	30	26,114	169	38	Geo R

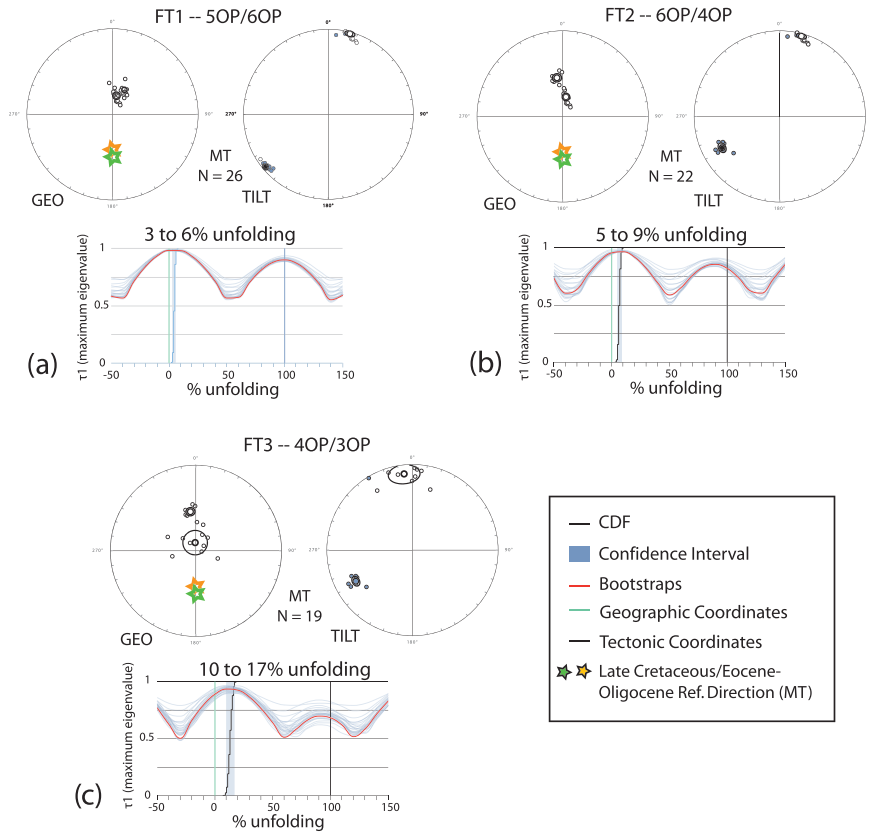
*Note.* Stable paleomagnetic components were defined in 23 out of the 29 sampled sites. Name of the considered component, number of samples used to calculate the site mean paleomagnetic direction ( $n$ ) from the total number of demagnetized samples ( $N$ ). Site mean directions are expressed as declination (D) and inclination (I) before (BTC) and after (ATC) tectonic correction plus the statistical parameters for a Fisherian distribution ( $\alpha_{95}$  and  $k$ ). Bedding is indicated as dip direction and dip, and dips higher than  $90^\circ$  indicate overturned bedding. The last column refers to the polarity (normal, N, or reverse, R) of the components before (geo) or after (tilt) tectonic correction (we chose the option where the component was closer to the reference direction). When dual polarities were defined at the site scale, the number of samples showing each polarity is indicated.

components in geographic coordinates, and (iii) their stronger scattering after bedding correction, we rely on the 0% maxima as those being consistent with the whole data set.

The absence of accessible, mesoscale or kilometric-scale folds in the Paleozoic and Mesozoic units of the northern Axial Zone prevented the application of fold tests in this domain. In these units, the most frequent component is the MT one. It displays normal and dual polarities in geographic coordinates (Figure 9d, Table 3) and a north-directed and moderately plunging orientation in geographic coordinates.

Considering the age of the sampled units and the fold test results, a Cretaceous to early Cenozoic age is roughly inferred for the MT remagnetization (timing of magnetization will be further discussed in section 6). Paleomagnetic references for the Pyrenean domain during this time span range between  $345.5^\circ/50.5^\circ$  ( $N = 2$ ,  $\alpha_{95} = 6.7^\circ$ ,  $k = 698.2$ ) for the Early Cretaceous to  $000^\circ/46^\circ$  ( $N = 4$ ,  $\alpha_{95} = 4.7^\circ$ ,  $k = 291$ ) for the Late Cretaceous and  $0^\circ/52^\circ$  ( $N = 4$ ,  $\alpha_{95} = 8.4^\circ$ ,  $k = 90.4$ ) for the early Cenozoic. Comparison between the direction of the obtained MT components and the Late Cretaceous and/or early Cenozoic reference directions (Figure 9) evidences a deviation in the inclination that is strong in the Mesozoic units of the CB (Figures 9a to 9c) but weaker or even null in the Paleozoic/Mesozoic units in the northern Axial Zone (Figure 9d). The origin of this inclination difference is addressed in section 6 of this work.

FOLDS IN THE CHAINONS BEARNAIS (Mesozoic units)



SITES IN THE AXIAL ZONE (Paleozoic and Mesozoic units)

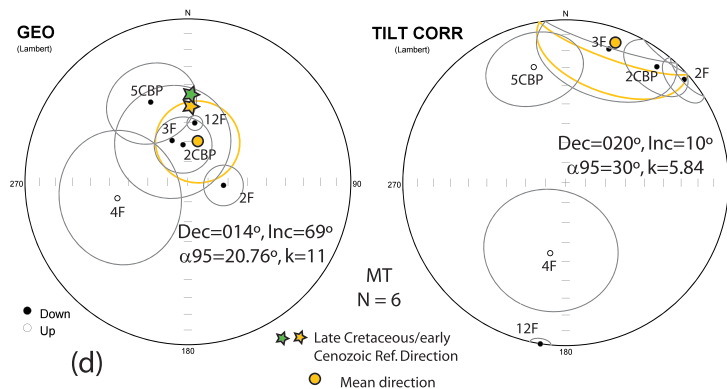


**Figure 9.** (a–c) Fold test (FT) results in the CB (see location of sites in Figure 3). Stereoplots show the orientation of the MT paleomagnetic component before (left) and after (right) tectonic correction. Both sample (N) and site mean components are shown. Underneath, results of stepwise fold tests (Tauxe & Watson, 1994) are shown with indication of the unfolding percentage at which the best grouping among components is attained. Site 3OP is transposed to reverse polarity in (c). The Late Cretaceous and early Cenozoic reference directions are shown (in geographic coordinates; hollow stars indicate the reference direction in reversed polarity). These reference directions were calculated for a common reference point centered at 43.04° and –0.35°. For the early Cenozoic reference, the paleopole position was calculated considering the average paleomagnetic orientation obtained in Taberner et al. (1999) and Gómez-Paccard et al. (2012) studies and their location. Afterwards, the expected declination and inclination were computed (from each individual paleopole) for the central position of our study area. Regarding the Cretaceous reference, we used the paleopole positions computed and compiled by Osete and Palencia-Ortas (2006). Folds in the CB have a limited along-strike extent and are not perfectly cylindrical, which can potentially lead to errors during unfolding (the direction of the postfolding component is not biased by these potential errors). (d) Average MT component (orange symbols) defined from site means (black symbols) in the northern Axial Zone, in geographic coordinates (left) and after tectonic correction (right). The Late Cretaceous and early Cenozoic reference directions are shown. Dual polarity sites (12F and 2CBP) were plotted as normal polarity sites in geographic coordinates. Mean directions were defined after transposing reverse polarity sites. Note that bedding orientation used to apply the tectonic correction in the Paleozoic sites probably results from the overprint of Cenozoic folding onto previous Variscan structures.

#### 5.2.4. Artificial TRM

When analyzing the direction of LT and MT components, we observe that 7 out of 18 sites display paleomagnetic components at an angle to bedding lower than  $20^\circ$  (Table 3). This raises the question of a possible bias in the paleomagnetic directions, similar to that observed by Fuller (1963) who reported a strong deviation of the NRM towards cleavage planes in slate samples, the deviated paleomagnetic component being carried by anisotropic pyrrhotite. To test this possibility, we designed a three-step laboratory experiment. As it will be discussed in section 6, both LT and MT components are likely thermoremanent magnetizations (TRM) that were blocked when the pyrrhotite was cooled from above its Curie temperature ( $\sim 320^\circ\text{C}$ ) to below it. To simulate this process, we imprinted an artificial TRM in two samples from sites 4OP and 5OP, where pyrrhotite carries the main paleomagnetic component that defined a low angle to bedding ( $17^\circ$  and  $10^\circ$ , respectively). We heated these samples at  $350^\circ\text{C}$  under a null magnetic field at a rate of  $30^\circ\text{C}/\text{min}$  to prevent against the alteration of the magnetic minerals. To this purpose, the heat transfer to the sample was achieved by means of FURMAG infrared-heating furnace (Poidras et al., 2012) mainly by radiation with a small part of conduction. Afterwards, samples were cooled down to room temperature in about 20 min while a magnetic field of  $80\ \mu\text{T}$  was applied at different angles with respect to bedding (from  $0^\circ$  to  $80^\circ$ ). We then measured the artificially created TRM and checked its consistency during stepwise thermal demagnetization up to  $350^\circ\text{C}$ . The full demagnetization of the TRM was reached at  $320^\circ\text{C}$ , implying that pyrrhotite is the magnetic carrier and that no additional magnetic minerals were produced upon initial heating at  $350^\circ\text{C}$ . The TRM (see Figure S3 in Supporting Information), artificially created at ambient pressure, is parallel within few degrees with the direction of the applied magnetic field, independently on its direction with respect to bedding.

These results suggest that no significant bias towards the bedding plane is affecting the pyrrhotite-carried components in the study area, as considered in previous studies dealing with TRM-like records in the Himalayan range (Appel et al., 2012; Crouzet et al., 2001).

## 6. Discussion

### 6.1. The Structuration of the CB: Constraints from Peak Temperatures and Paleomagnetic Record

#### 6.1.1. Peak Temperatures and Isotherms Geometry

Peak temperatures in the Northern Pyrenees are related to extreme continental thinning during the Cretaceous and indicate that this episode was characterized by high geothermal gradients ( $\sim 60$  to  $80^\circ\text{C}/\text{km}$ , Chelalou et al., 2016; Ducoux et al., 2019; Hart et al., 2017; Vacherat et al., 2014). In the study area, peak temperatures vary between  $\sim 330^\circ\text{C}$  and  $\sim 480^\circ\text{C}$ , being similar to the RSCM peak temperatures defined in the Baronnies-Barouse area (Clerc et al., 2015), located about 30 km to the east and slightly higher than maximum RSCM temperatures in the Mauléon domain, 30–40 km to the west ( $300$ – $400^\circ\text{C}$ ; Clerc et al., 2015). Our new temperatures fit the westwards temperature decrease along the North Pyrenean Zone defined by previous studies (Clerc et al., 2015), although this trend is abruptly interrupted further west (in the Basque Pyrenees) where peak temperatures exceed  $550^\circ\text{C}$  (Ducoux et al., 2019). Apart from the E-W variation in Cretaceous peak temperatures, previous data in the Eastern Pyrenees also indicate an N-S zonation, with the highest temperatures being limited to the southernmost area of the North Pyrenean Zone and the northern domains being characterized by a rapid decrease of the metamorphic imprint (Clerc et al., 2015). This N-S gradient can also be defined from the data set presented in this work, with peak temperatures decreasing to the north from a temperature maximum located in the southern CB and the northern Axial Zone ( $\sim 390^\circ\text{C}$  to  $\sim 480^\circ\text{C}$ ).

Calculated peak temperatures (Table 1) are independent on the stratigraphic position of the samples (see Figure S2 in Supporting Information) and are almost homogeneous ( $\sim 340$ – $360^\circ\text{C}$ ) across the area where the Montcaou anticline and the lateral continuation of the Mail Arrouy structure crop out (Figure 6). In the Paleozoic basement, a main difference has been established between the Pic de Bazès-Arbéost unit (higher temperatures,  $\sim 370$ – $450^\circ\text{C}$ ) and the Eaux-Bonnes unit ( $\sim 320$ – $350^\circ\text{C}$ ). Note that sample sites in the Paleozoic are away from late Variscan intrusive bodies or Permian volcanics (located in the Eaux-Chaudes unit, Figure 3) and that obtained RSCM temperatures are significantly (Pic de Bazès-Arbéost unit) or slightly higher (Eaux-Bonnes unit) than those expected from the low-grade Variscan metamorphism affecting the western Axial Zone ( $< 300^\circ\text{C}$ ; Ternet et al., 2004). This discards a Paleozoic age for

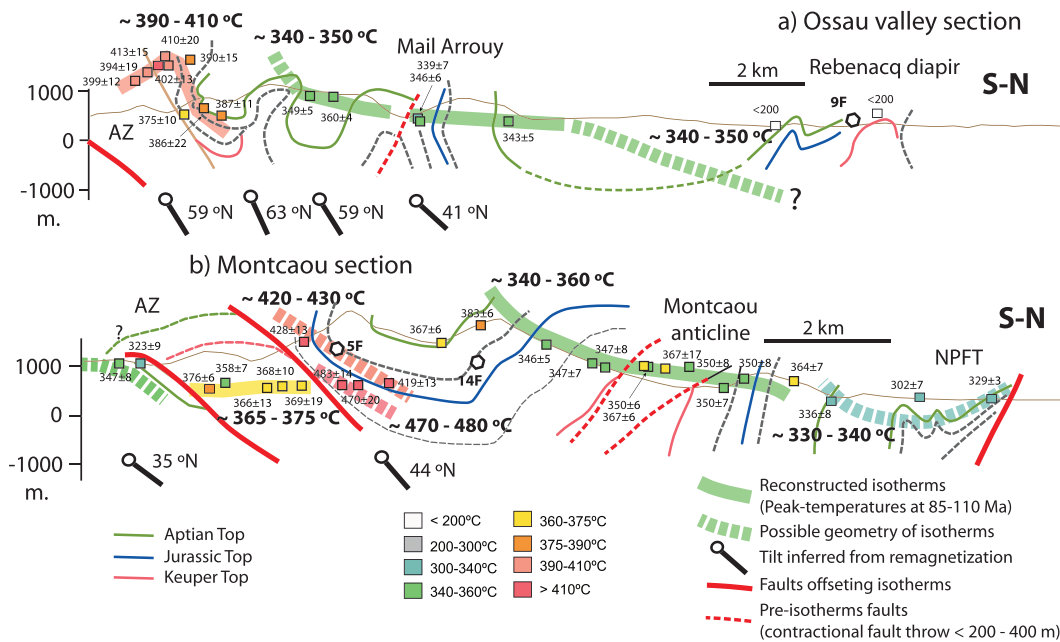


**Figure 10.** Schematic cross-sections across the Ossau valley (a) and the Montcaou structure (b) with projection of peak temperatures estimates (only data from thin sections are considered, from sites located at a distance lower than 4–5 km from the studied transects). Values in the lower part of the sections indicate late tilting deduced from paleomagnetic data (see details in section 6.2).

the peak temperatures in the northernmost Axial Zone (Pic de Bazès-Arbéost unit) that cannot be completely ruled out in the sites along the Eaux-Bonnes unit showing peak temperatures close to 300°C.

To better constrain the relationship between peak temperatures, folding, and thrusting, we projected RSCM data on the previously described cross-sections (Figure 10) and reconstructed the first-order geometry of isotherms in cross-section view. RSCM data were projected considering the orientation of fold axis across the study area. Only peak temperature data of clear mid-Cretaceous age (the Eaux-Bonnes unit was discarded) and from sites located on or close (<5 km) to the cross-sections were considered. Given the variability and standard deviation of peak temperature values, defined isotherms represent temperature ranges of ~10–20°C that can increase to ~30°C if the inherent RSCM calibration error is considered (Beysac et al., 2002).

In the southern part of the Ossau valley cross-section (Figure 10a), we depicted a 390–410°C isotherm that is shallowly south dipping along the northernmost portion of the Axial Zone and then dips steeply to the north in the southernmost part of the CB. RSCM data point out that this isotherm is folded but not shifted along the contact between Paleozoic and Mesozoic units. To the north, the 340–350°C isotherm is inferred to dip shallowly to the north (10–15°), cutting across the Mail Arrouy structure (Figure 10a).

Across the Montcaou section (Figure 10b), a flat ~365–375°C isotherm can be depicted in the Paleozoic units of the northern Axial Zone at approximately the same altitude as the ~470–480°C isotherm in the Mesozoic units that crop out immediately to the north. This significant shift (i.e., ~100°C) of the isotherms suggests that the contact between the Paleozoic basement and its Mesozoic sedimentary cover behaved as a south-directed thrust after peak metamorphism (i.e., during the late Mesozoic–Cenozoic contractional stages). As the 390–410°C isotherm in the Ossau section, the ~470–480°C and ~420–430°C isotherms in the southernmost Mesozoic units of the Montcaou profile dip to the north, although the sparse distribution of samples in this part of the cross-section prevents the precise geometrical characterization of isotherms (depicted as dotted lines in Figure 10b). Northwards, peak temperatures decrease, and the ~340–360°C isotherm dips ~20–25° to the north in the southern limb of the Montcaou anticline and flattens in its northern limb, crosscutting folded units and associated faults. Across the North Pyrenean frontal thrust, lower temperatures were measured, and although isotherms cannot be accurately defined, a constant northwards dip is inferred for them across the Ossau section, whereas they are probably folded in the hanging wall of the North Pyrenean frontal thrust across the Montcaou section (see the syncline depicted in Figure 10b).

This latter geometry indicates a postmetamorphic folding and offset of the isotherms in the hanging wall of the North Pyrenean frontal thrust that is consistent with the reactivation of this structure as a north-directed thrust during the late Mesozoic-Cenozoic.

To sum up, RSCM data suggest that isotherms comprised between  $\sim 330\text{--}480^\circ\text{C}$  cut across the small- and intermediate-wavelength folds (1 to 4 km) affecting the southern CB in the study area (the Montacou and Béon anticlines, the Mail Arrouy structure, and the Jaout syncline; see location in Figure 3). This crosscutting relationship between isotherms and folds can be considered as an indication of the relative age between them, the isotherm imprint postdating the folding. Similar relative time relationships between isotherms and cover folds have been reported in the Basque-Cantabrian Pyrenees (Ducoux et al., 2019). Based on the absolute age of high-temperature metamorphism (i.e., 85–110 Ma, mostly obtained by  $^{40}\text{Ar}\text{--}^{39}\text{Ar}$  and U–Pb dating methods on metamorphic and magmatic minerals; see Clerc et al., 2015 and references therein), we can propose that these folds were mostly formed during syn-rift stages in the Northern Pyrenees (i.e., in Jurassic to Early to mid-Cretaceous), before the onset of contraction. This folding age is consistent with the thickness variations, rapid facies changes, and major unconformities observed in the Jurassic to Early Cretaceous sedimentary sequence (Figures 3, 4, and 5). They attest for an early and long-lasting structuring of the sedimentary cover that is affected by early salt structures as observed further north in the Aquitaine basin where contractional deformation is less important (e.g., Biteau et al., 2006; Canérot et al., 2005).

Peak temperature isotherms in the study area were later deformed by a larger-wavelength folding: they are flat or shallowly south dipping in the northernmost Axial Zone, steeply or moderately dipping in the southernmost CB (where they are partly transported onto the northern Axial Zone, Figure 10b) and flat to shallowly dipping in the northern CB and the North Pyrenean frontal thrust domain. This large-scale folding roughly mimics the basement top geometry depicted in the studied cross-sections (compare sections in Figures 4 and 12), which suggests that syn-contractional basement faulting and folding are the main mechanisms deforming peak temperature isotherms after the peak metamorphic stage.

### 6.1.2. Constraints From Paleomagnetic Data

#### 6.1.2.1. Remagnetization in the Northern Pyrenees

Remagnetizations in the Northern Pyrenees have been previously described both to the east (Corbières area, Rouvier et al., 2012) and to the west (Mauléon basin, Oliva-Urcia et al., 2010) of the study area. In the Mauléon Basin (distant by  $\sim 40$  km from our study area), Oliva-Urcia et al. (2010) documented a remagnetized area affected by both HT and MT components, carried by magnetite and iron sulphides, respectively. These magnetite and iron sulphides components show normal and reversed polarities in geographic coordinates, respectively, both postdate folding, and display a strong clockwise deviation in the declination with respect to the reference direction.

The paleomagnetic data set presented in this study confirms the widespread occurrence of late remagnetizations in the Mesozoic units of the North Pyrenean Zone and documents that these remagnetizations also affect the Paleozoic units in the northern Axial Zone. Similarly to the Mauléon Basin (Oliva-Urcia et al., 2010), remagnetization in the study area resides both in magnetite and pyrrhotite. Pyrrhotite-carried components are mostly postfolding and display a dominant reverse polarity in geographic coordinates across the CB (10 out of 12 sites for the MT component, Table 3), whereas dual polarities have been defined in the northern Axial Zone. They are deviated in inclination but not so strongly in declination from the expected reference directions.

The comparison between the distribution of pyrrhotite- and magnetite-carried remagnetizations and RSCM temperatures evidences a good correlation between them: pyrrhotite is present in areas where peak temperatures are  $>330^\circ\text{C}$ , whereas magnetite occurs where peak temperatures are  $<340^\circ\text{C}$  (Table 2, see magnetite and pyrrhotite windows in Figure 11, from Aubourg et al., 2019). Pyrrhotite, in its monoclinic form ( $\text{Fe}_7\text{S}_8$ ), is a common secondary mineral in low-grade metamorphic rocks (Appel et al., 2012; Crouzet et al., 2001; Crouzet, Ménard, & Rochette, 2001; Gillett, 2003; Lambert et al., 1998; Rochette et al., 1990; Schill et al., 2004; Wehland et al., 2005). Pyrrhotite results from the breakdown of magnetite and pyrite by a temperature of  $\sim 200^\circ\text{C}$  (Gillett, 2003; Rochette, 1988). When magnetite transforms to pyrrhotite, the magnetite-carried magnetization is partly or fully replaced by a pyrrhotite-carried remagnetization (Aubourg et al., 2012, 2019) whose nature will depend on the peak temperature reached during burial (see Appel et al., 2012). If temperature is higher than the Curie temperature of pyrrhotite ( $\sim 320^\circ\text{C}$ ), a

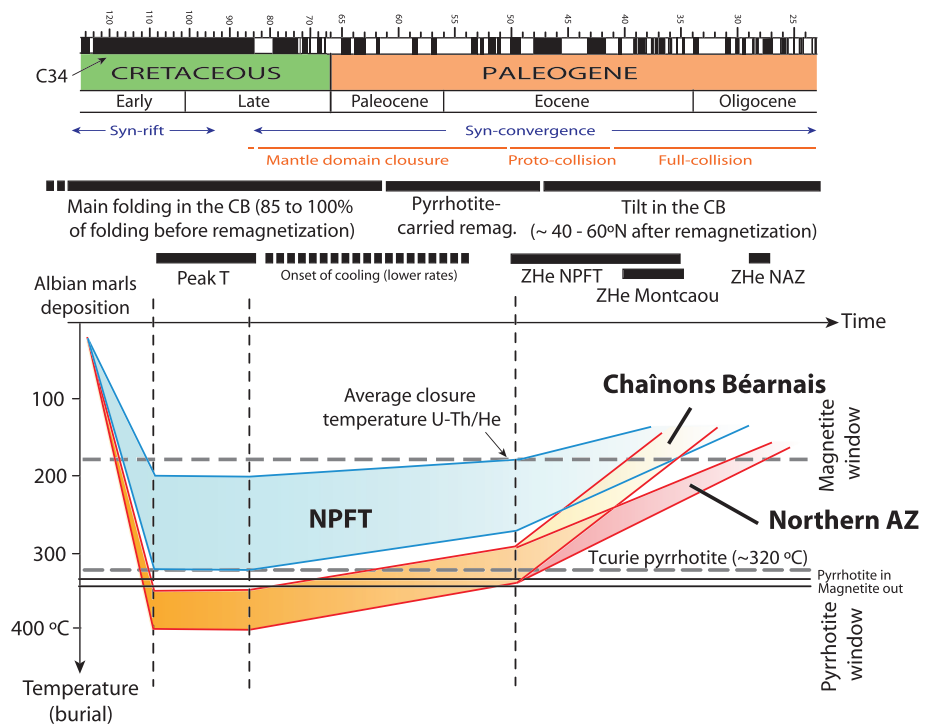


**Figure 11.** Timing of main tectonic, thermal, and magnetization events in the CB and northern Axial Zone (from Early Cretaceous). The magnetic polarity time scale is from Gradstein et al. (2012). Peak metamorphism age (peak T) is from Clerc et al. (2015). ZHe ages (Bosch et al., 2016) are interpreted as cooling ages below 220–140°C.

TRM will develop during cooling. This is the case in the studied area, where the peak temperature range defined in the northern Axial Zone and the CB is usually higher than the Curie temperature of pyrrhotite, suggesting that the pyrrhotite-carried remagnetization is a TRM that was locked during the cooling of the sampled units below 320°C.

#### 6.1.2.2. Age of the Remagnetization

In the study area, the polarity of remagnetizations helps in constraining the age of remagnetization events. The polarity of the MT remagnetized component across the CB is dominantly reverse, as also defined in the Mauléon Basin (Oliva-Urcia et al., 2010). This reverse polarity indicates that the pyrrhotite-carried remagnetization was locked after the long C34 normal polarity chron (124–84 Ma) (Gradstein et al., 2012), coevally to plate convergence stages (Figure 11).

Previous studies in the Western Pyrenees (Gómez-Romeu et al., 2019; Teixell et al., 2016) have proposed three successive stages during the convergence between the Iberian and Eurasian plates (Figure 11). The early convergence was first accommodated by the closure of the exhumed mantle domain followed by the overriding of the thinned Iberian margin on top of the European margin, probably starting during Early Eocene times (proto-collision in Figure 11). During these early stages, the continental crust progressively recovered its original thickness before the continental collision by Late Eocene times (Gómez-Romeu et al., 2019; Teixell et al., 2016). The timing of these convergence stages is partly constrained by low-temperature thermochronology data in the central-western Pyrenees that evidence rapid cooling at ~50 Ma in the Mauléon Basin (Vacherat et al., 2014). In our study area, (U-Th)/He dating on zircon (ZHe) yielded ages of ~35–50 Ma in the hanging wall of the North Pyrenean frontal thrust, of ~34–39 Ma in the Montcaou anticline, and ~27–29 Ma in the northernmost Paleozoic units of the Ossau valley (Bosch et al., 2016), which may be interpreted as cooling ages below a closure temperature range of 140°C to 200–220°C (Bosch et al., 2016; Guenther et al., 2013). Because the closure temperature of (U-Th)/He system in zircon is lower than the blocking temperature of pyrrhotite (~320°C), the age of the remagnetization carried by the latter has to be older than the ZHe ages, probably during the early Paleogene (Paleocene–early Eocene), coevally with the closure of the exhumed mantle domain (Figure 11). Differences in the cooling

**Table 4**  
Calculation of Horizontal Axis Rotations (HARs) or Tilts and Related Uncertainties ( $\Delta$ HAR)

Sites	Dec. MT BFD	I MT BFD	$\alpha_{95}$	HAR	$\Delta I_{\text{obs}} (\alpha_{95})$	$\Delta I_{\text{ref}}$	$\Delta$ HAR
<b>MT component in the Mesozoic units of the Chaînons Béarnais</b>							
5OP/6OP (FT1, BFD geo)	19.6	-68.8	2.6	59.2N	2.6	8.4	11
6OP/4OP (FT2, BFD 10%unfold)	355.1	-64.9	4.2	63.1N	4.2	8.4	12.6
4OP/3OP (FT3, BFD 10%unfold)	340.6	-68.8	6.8	59.2N	6.8	8.4	15.2
3OP/7OP (FT5, BFD geo)	114.3	79.9	9.9	41N	9.9	8.4	18.3
5F/14F (FT6, BFD geo)	218.9	83.2	12.6	44N	12.6	8.4	21
<b>MT component in the Paleozoic and unconformably overlying Mesozoic units of the northern Axial Zone</b>							
12F	6.5	59.9	3.8	8S	3.8	8.4	12.2
5CBP	335.1	44.8	21.3	8N	21.3	8.4	29.7
2CBP	172.6	-71	14.2	20N	14.2	8.4	22.6
2F	94.8	72.2	10	35N	10	8.4	18.4
3F	339.3	67.6	28.8	16N	28.8	8.4	37.2
4F	257.4	-53.4	32.3	4S	32.3	8.4	40.7

Note. For MT components (postfolding to late syn-folding), horizontal axis rotations were obtained from the comparison of the orientation of MT in geographic coordinates (Declination, Dec, and Inclination, Inc) or at the best fit direction (BFD) obtained from fold test (FT) results and that of the early Cenozoic reference direction (Dec = 000°, Inc = 52°,  $\alpha_{95}$  = 8.4°,  $k$  = 90.4). Gray cells indicate statistically significant HARs.

age of the different structural units are consistent with the changes in the polarity of the MT component: it is essentially reverse across the CB, whereas both normal and dual polarities are frequent across the northern Axial Zone. These changing polarities indicate a diachronous cooling, being probably younger in the Axial Zone than in the Northern Pyrenees (as also suggested by thermochronology data; Bosch et al., 2016).

Taking the early Paleogene as the most probable time interval for the blocking of the pyrrhotite-carried remagnetization in the study area (note the prevalence of reverse polarity chrons during this time span, Figure 11), and considering the fold test results for MT components in the CB (Figures 9a to 9c), we can quantitatively define that ~85–100% of the fold limb dips were acquired before the collisional stage in the Western Pyrenees. By considering this relative time constraint together with (i) the crosscutting relationship between peak temperature isotherms (dated at 85–110 Ma) and the short- to intermediate-wavelength folding of the sedimentary cover (Figure 10) and (ii) thickness variations and unconformities in the Jurassic–Lower Cretaceous units, we propose that the main folding event in the study area took place before contractional times (Figure 11).

#### 6.1.2.3. Horizontal Axis Tilts Deduced From Paleomagnetic Data

The large-wavelength folding of the isotherms and the deviated paleomagnetic directions in the CB evidence a late folding stage that took place after the locking of the pyrrhotite-carried remagnetization. This late folding can be quantified through the comparison of the remagnetization direction (MT component) and the early Cenozoic reference (Dec = 0°, Inc = 52°,  $\alpha_{95}$  = 8.4°,  $k$  = 90.4, see section 5.2.3) that indicates relatively slight inclination differences in the Paleozoic units of the Axial Zone (Figure 9d) and strong inclination deviations across the CB (Figures 9a to 9c). Inclination differences in the Mesozoic units (see calculations in Table 4) result from a late steepening of paleomagnetic directions attaining: (i) ~60° to the north in the southern CB across the Ossau valley and (ii) ~40–45° to the north in the Jaout syncline and the Mail Arrouy structure (Montcaou cross-section, tilt values are indicated in Figure 10). Regarding the Paleozoic units, postremagnetization tilts are shallow to the south (from 4° to 8°) and shallow to moderate to the north (8 to 35°), although these tilts are not statistically significant except in site 2F (35° ± 18°). These tilts likely result from the rotation of units about a horizontal axis that parallels to ~E-W-striking fold axis and thrust planes in the study area.

Horizontal axis tilts in the southern part of the Montcaou section (~44° to the north) equal the dip (~45°N) of the Lower Triassic units unconformably overlying the Paleozoic basement in the hanging wall of the Pic de Bazés-Arbèost thrust (see section 3) and are roughly subparallel to the ~420–430°C and ~470–480°C isotherms reconstructed from RSCM data in that portion of the cross-section (Figure 10b). Similarly, tilts in the southern part of the Ossau valley cross-section (~60° to the north) are similar to the dip of the ~390–410°C isotherm defined in this area (Figure 10a). Tilts defined from the Paleozoic samples in the hanging

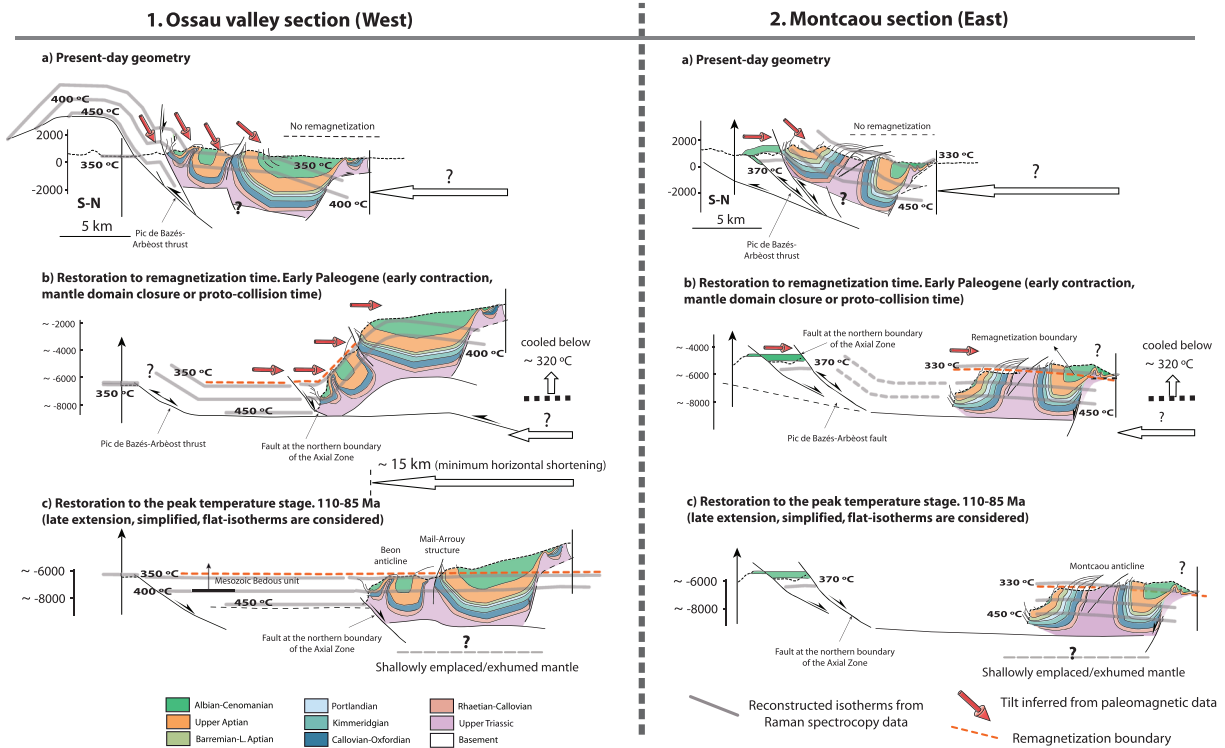


**Figure 12.** Stepwise restorations of the Ossau (left) and Montcaou (right) cross-sections at the time of remagnetization (early shortening stages predating full continental collision, b) and at the time of peak temperatures (final extensional stages, c). Deformation depths are roughly calculated considering peak temperature values and the blocking temperature for the pyrrhotite-carried remagnetization ( $\sim 320^{\circ}\text{C}$ ) and assuming a  $50^{\circ}\text{C}/\text{km}$  geothermal gradient during peak metamorphism that could decrease to  $40^{\circ}\text{C}/\text{km}$  in the early contractional stages predating the recovery of the normal continental crust thickness and the full continental collision.

wall of the Pic de Pic de Bazés-Arbèost thrust (Ossau valley cross-section) are conversely more limited, in agreement with the proposed flat or shallowly dipping isotherms and accordingly to the dip of the Cretaceous in this unit (Figure 4a). The good agreement between horizontal axis tilts, isotherms dips, and dip of the Mesozoic units unconformably overlying the Paleozoic basement points out that the rotation of the remagnetized component and of the peak temperature isotherms mainly results from basement tilting and folding. Inferred tilts are mainly to the north, accordingly with the location of the sample sites in the back limb of the Axial Zone basement thrust system (Figures 1b and 3).

### 6.2. Towards a Kinematic Scenario for the CB: Constraints on the Evolution of the Cover and Shallow Basement Structure

Based on the presented data sets here, the Ossau valley and Montcaou cross-sections were restored to the pyrrhotite-carried remagnetization and peak temperature times (Figure 12) that, following the previously suggested and published ages, correspond to the early convergence and the late extensional stages in the study area, respectively (Figure 11). Cross-sections were restored from a pin line located in the footwall of the Pic de Bazés-Arbèost thrust (Figure 12a; see location in Figure 3). They refer to the structure of the Mesozoic cover and the shallower basement, but the deep structure of the CB remains unresolved.

Cross-section restorations were carried out in two steps. In the first step (remagnetization time, Figure 12b), isotherms and folds were restored using paleomagnetic data as a paleohorizontal marker (i.e., we back tilted the horizontal axis rotations calculated from the comparison between the MT remagnetization and the early Cenozoic reference direction, Table 4). The second restoration step was achieved by flattening the peak temperature isotherms (Figure 12c). We acknowledge that horizontal isotherms represent a simplification of the temperature field in a hyperextended margin involving salt units. Isotherms in these settings are likely

deflected from a flat geometry by (i) short wavelength thermal anomalies related to the high thermal conductivity of the salt (Kaiser et al., 2011) and/or (ii) long wavelength anomalies related to the lateral variation of crustal thicknesses and mantle depths across the margins (Brune et al., 2014; Duretz et al., 2016). Salt-related anomalies are estimated to be less than 10°C in supra-salt units (Grunnaleite & Mosbron, 2019; Jensen, 1983) and are thus below the resolution of the isotherms defined in this work (10–20°C uncertainty) and the inherent uncertainty of the applied geothermometer (~30°C). Crustal and mantle depth-related anomalies consist of a 100-s-km bend of the isotherms towards the rift axis, characterized by a <10° outward dip across the hyperextended domain (e.g., Brune et al., 2014; Duretz et al., 2016). Given the small magnitude of both the crustal-related and the salt-related thermal anomalies expected in the studied scenario, the spatial scale of our restored cross-sections (~20 km), and the uncertainty on the obtained RSCM temperatures and isotherms, we consider that the flat isotherms depicted in Figure 12c represent a simplified but appropriate approximation to the original thermal configuration of the Cretaceous basin in the Northern Pyrenees. To complete the restorations, fault displacements were restored by joining isotherms in their side blocks. An inherent uncertainty of 150 to 300 m in fault throws has to be considered because of the 10–20°C temperature uncertainty of the reconstructed isotherms (maximum of ~425 m, considering the ~30°C RSCM calibration error and an average geothermal gradient of 70°C/km, Chelalou et al., 2016; Ducoux et al., 2019; Hart et al., 2017; Vacherat et al., 2014). The present-day topography line (dotted black line in Figure 12) was also passively restored using remagnetization and peak temperature isotherms.

Restorations to the peak temperature time (late extensional stages, Figure 12c) evidence a folded Mesozoic cover in the CB in the late Aptian–Coniacian. The geometrical relationship between peak temperature isotherms and bedding across the Montcaou, Mail Arrouy, and Béon anticlines indicates that these folds were already developed at this stage. At this time (late Aptian–Coniacian), they consisted of upright to north-verging folds with steep limbs, the Montcaou and Mail Arrouy structures displaying a longer wavelength than the Béon anticline. The smaller-scale folds observed in the Aptian limestones of the southern CB (Ossau valley cross-section, Figure 5d) could potentially be second-order folds related to these larger-wavelength structures. Early folding in the CB has been proposed to result (at least partly) from the gravity gliding of the Mesozoic cover above the Triassic salt (Lagabrielle et al., 2010). This mechanism has been recognized in other areas of the Pyrenees (Espurt et al., 2019; López-Mir et al., 2015; McClay et al., 2004; Saura et al., 2016). Gravity gliding can trigger coeval extensional and contractional structures that develop updip and downdip the detachment level, respectively (Rowan et al., 2004 among others). The contractional structures in the downdip area can correspond to tight, upright, or doubly verging folds (Brun & Fort, 2011; McClay et al., 2003) such as those we propose in the restoration to the peak temperature stage (Figure 12c). Besides gravity gliding, differential sedimentary loading (because of thickness variations in the Jurassic and Lower Cretaceous sequence) probably played a major role in early salt withdrawal and folding of the CB, as recognized further west in the Parentis Basin (Ferrer et al., 2012) and the Basque-Cantabrian Pyrenees (Bodego et al., 2018).

During extensional stages (Figure 12c), the boundary between the Paleozoic units of the future Axial Zone and the Mesozoic of the CB was represented by an extensional shear zone (i.e., the penetratively foliated zone observed in the Mesozoic of the southern CB, Ossau valley cross-section, Figure 5c). To the south, the Cretaceous basin expanded and the Pic de Bazès-Arbéost structure probably corresponded to the proximal basin environment, with Cenomanian units consisting of marls and limestones with interbedded breccias and conglomerates (Ternet et al., 1980). To the north, in the CB domain, the presence of lherzolites embedded within the Keuper units along the hinge zone of the Montcaou and Mail Arrouy structures (Figure 3) points out that the mantle was exhumed or emplaced at a very shallow level (Clerc et al., 2012; Corre et al., 2018; Lagabrielle et al., 2010; Pedrera et al., 2017; Teixell et al., 2016; Wang et al., 2016). Further north, in the North Pyrenean frontal thrust domain, the thinning of the Jurassic and Lower Cretaceous sequence, together with the peak temperatures decrease (Figure 6), suggests that the Cretaceous basin floor was uplifted in this area (Figure 4). This basement uplift could laterally connect to the Grand Rieu High to the west (Hart et al., 2017; Teixell et al., 2016).

The restoration at the pyrrhotite-carried remagnetization time (early contractional stages, Figure 12b) depicts how the early inversion was resolved in the CB. This remagnetization was blocked during slow

cooling associated with mantle domain closure or early proto-collision stages (Figure 11). Fold tests evidence that fold limbs in the Béon and Mail Arrouy structure had already acquired 85% to 100% of their dip before the remagnetization time. Combined with the crosscutting relationships between the peak temperature isotherms and the fold limbs, this result suggests that the interlimb angles in these structures have remained mostly constant from the peak temperature stage to the present day (Figure 12). In this scenario, moderate fold tightening during contraction could occur through faulting in the hinge zones of the salt domes. Such a faulting did not shift isotherms and was therefore probably below the uncertainty range of the reconstructed isotherms (i.e., fault throws below ~425 m). Besides, a contractional or partly contractional origin cannot be ruled out for the minor folds to the north of the Montcaou structure where no paleomagnetic nor thermal data constrain fold evolution through time.

Early shortening was mostly accommodated by the closure of the exhumed mantle domain (Jammes et al., 2009; Jourdon et al., 2020; Lagabrielle et al., 2010; Masini et al., 2014; Tugend et al., 2014) and the reactivation of early extensional basement faults in the southern basin margin (these extensional faults could locally be preserved, Figures 5a and 5b) as top to the south thrusts. Reactivated faults transported passively the early folded cover in the CB in their hanging wall. In the Montcaou section, the isotherms shift at the boundary between the northern Axial Zone and the CB points out that shortening produced the inversion of the extensional fault found at this location (Figure 12, 2b). On the contrary, the restoration of the Ossau valley cross-section proposes that contraction was mostly resolved through the inversion of the Pic de Bazès-Arbéost fault that produced an early folding of the isotherms and the inherited Cretaceous folds in its hanging wall (Figure 12, 1b). Latter contraction was probably accommodated by thrusting along these two faults (the fault at the contact between the CB and the northern Axial Zone and the Pic de Bazès-Arbéost fault) and by the initiation of subsequent basement thrusts in their footwalls (compare stages a and b in Figure 12). Basement thrusting produced the stack of basement units and the strong northwards tilt of the folded Mesozoic sequence in the CB. Tilt values range between  $63^{\circ} \pm 13^{\circ}$  and  $41^{\circ} \pm 18^{\circ}$  and have been successfully quantified thanks to the paleomagnetic record (Table 4, Figure 10). Regarding the northern CB basin margin, thermal estimates indicate a minor inversion along the North Pyrenean frontal thrust, especially to the west where the low peak temperatures ( $<200^{\circ}\text{C}$ ) both in the hanging wall and the footwall of this structure indicate a limited displacement (the Rebenacq diapir, Figure 6). To the east, the peak temperatures slightly increase and the  $\sim 330\text{--}340^{\circ}\text{C}$  isotherm is folded and uplifted in the hanging wall of the North Pyrenean frontal thrust (considering the footwall of the thrust as reference, Figure 10), suggesting an eastward increase in the vertical motion of this thrust.

A minimum shortening value in the Ossau valley cross-section (Figure 12.1) of ~15 km was estimated considering (i) the Pic de Bazès-Arbéost thrust geometry depicted in Figure 4b and (ii) the peak temperature values in the footwall and the hanging wall of this thrust (from this and previous studies; see Figure 6). Displacement in the North Pyrenean frontal thrust is not considered, and there are no constraints to define the percentage of shortening accommodated before and after the remagnetization event (i.e., early Paleogene). Nevertheless, the absence of significant vertical axis rotations in the study area (i.e., the declination of paleomagnetic vectors is consistent across the two considered sections and with the declination of the early Cenozoic reference) suggests that the postremagnetization shortening was similar across the two studied profiles (Figure 12). Note that these minimum shortening estimates could attain erroneous values of ~23 km if the Cretaceous horizons are completely unfolded at the time of extension.

## 7. Conclusions

This work provides an extensive data set of paleomagnetic and RSCM peak temperatures throughout the CB and the northern Axial Zone, in the Northern Pyrenees. Based on these two independent constraints, we restored deformation geometries across two different cross-sections (the Montcaou and Ossau valley cross-sections) and semiquantitatively demonstrate that folding across the CB mostly took place before the onset of continental collision.

Peak temperatures in the study area were reached during the mid-Cretaceous (110–85 Ma) and led us to reconstruct almost straight isotherms that crosscut folds and faults affecting the Mesozoic units of the CB.

This crosscutting relationship suggests that most of these cover structures were formed before the record of this thermal event.

Paleomagnetic data reveal that the studied area is affected by a widespread remagnetization carried by pyrrhotite that was blocked after fold limbs had acquired the ~85% to 100% of their dip. A good correlation between >350°C peak temperatures and the occurrence of this remagnetization points out that it is a TRM acquired during the cooling of the sampled units. Considering the age of peak temperatures and previously published low-temperature thermochronological data, we estimated an early Paleogene age for the remagnetization, meaning that folding in the CB was essentially completed before collisional stages.

The early folding (Jurassic to Early to mid-Cretaceous) in this domain is consistent with field observations such as the thinning of Jurassic and/or lower Aptian units towards the hinge zones of anticlines or the presence of Lower Cretaceous units unconformably overlying older, early folded units. Contractual folding across the CB is revealed to be very limited, and Cenozoic shortening in the shallow basement units is shown to be resolved through the reactivation as south-directed thrusts of the extensional structures along the southern margin of the Cretaceous basin. These faults passively transported the folded CB in their hanging wall. Basement thrusting produced a strong northwards tilt (ranging between  $63^\circ \pm 13^\circ$  and  $41^\circ \pm 18^\circ$ ) of the folded Mesozoic sequence in the CB. This study evidences that the proper characterization of salt-cored, syn-extensional folding strongly controls the reliability of orogenic shortening estimates in fold-and-thrust systems reactivating previous extensional basins.

#### Acknowledgments

The authors acknowledge the support of Sonia Rousse, Melina Macouin, Juanjo Villalain, Pablo Calvin, Elisa Sánchez and Thierry Poidras in the Paleomagnetism Laboratories of the GET (Toulouse) and the Universities of Burgos and Montpellier. Jean-Baptiste Cuyala, Geoffrey Motte and Julia Lechantre are also thanked for their valuable help on the field and acquisition of Raman spectra. Esther Izquierdo-Llavall acknowledges the E2S UPPA postdoctoral contract in which the present study is framed and JP Callot acknowledges funding of the Structural Geology Chair at UPPA by Total SA. Funding from the CNRS program SYSTER is also acknowledged as well as Midland Valley for providing the Move academic license that was used for the construction of the cross-sections presented in this work. FURMAG rapid furnace construction was supported by the French National Agency for Research (ANR-12-BS06-0015). The data used in this work are listed in the references, text, tables, and figures in the manuscript and the supporting information. Samples are registered in SESAR (<https://www.geosamples.org/catalogsearch>), and paleomagnetic and RSCM results are publically available in the Mendeley Data Repository (<https://data.mendeley.com/datasets/sybybg5ymd/1>). We thank the careful review by Djordje Grujic (associate editor) and three anonymous reviewers who helped us to significantly improve the present manuscript.

#### References

- Aoya, M., Kouketsu, Y., Endo, S., Shimizu, H., Mizukami, T., Nakamura, D., & Wallis, S. (2010). Extending the applicability of the Raman carbonaceous-material geothermometer using data from contact metamorphic rocks. *Journal of Metamorphic Geology*, *28*(9), 895–914. <https://doi.org/10.1111/j.1525-1314.2010.00896.x>
- Appel, E., Crouzet, C., & Schill, E. (2012). Pyrrhotite remagnetizations in the Himalaya: A review. *Geological Society, London, Special Publications*, *371*, SP371–SP371. <https://doi.org/10.1144/sp371.1>
- Aubourg, C., Jackson, M., Ducoux, M., & Mansour, M. (2019). Magnetite-out and pyrrhotite-in temperatures in shales and slates. *Terra Nova*, *31*(6), 534–539. <https://doi.org/10.1111/ter.12424>
- Aubourg, C., & Pozzi, J. P. (2010). Toward a new < 250 °C pyrrhotite–magnetite geothermometer for claystones. *Earth and Planetary Science Letters*, *294*(1–2), 47–57. <https://doi.org/10.1016/j.epsl.2010.02.045>
- Aubourg, C., Pozzi, J. P., & Kars, M. (2012). Burial, claystones remagnetization and some consequences for magnetostratigraphy. *Geological Society, London, Special Publications*, *371*, SP371–SP374. <https://doi.org/10.1144/sp371.4>
- Barnett-Moore, N., Hosseinpour, M., & Maus, S. (2016). Assessing discrepancies between previous plate kinematic models of Mesozoic Iberia and their constraints. *Tectonics*, *35*, 1843–1862. <https://doi.org/10.1002/2015TC004019>
- Barnolas, A., Gil-Peña, I., Alfageme, S., Ternet, Y., Baudin, T., & Laumonier, B. (2008). *Mapa geológico de los Pirineos a escala 1:400 000*. IGME/BRGM ISBN: 978-2-7159-2168-9. Madrid and Orléans: IGME/BRGM.
- Beysac, O., Goffé, B., Chopin, C., & Rouzaud, J. N. (2002). Raman spectra of carbonaceous material in metasediments: A new geothermometer. *Journal of Metamorphic Geology*, *20*(9), 859–871. <https://doi.org/10.1046/j.1525-1314.2002.00408.x>
- Biteau, J. J., Le Marrec, A., Le Vot, M., & Masset, J. M. (2006). The Aquitaine basin. *Petroleum Geoscience*, *12*(3), 247–273. <https://doi.org/10.1144/1354-079305-674>
- Bodego, A., Iriarte, E., López-Horgue, M. A., & Álvarez, I. (2018). Rift-margin extensional forced folds and salt tectonics in the eastern Basque-Cantabrian rift basin (western Pyrenees). *Marine and Petroleum Geology*, *91*, 667–682. <https://doi.org/10.1016/j.marpetgeo.2018.02.007>
- Bosch, G. V., Teixell, A., Jolivet, M., Labaume, P., Stockli, D., Domenech, M., & Monie, P. (2016). Timing of Eocene–Miocene thrust activity in the Western axial zone and Chainons Béarnais (west-Central Pyrenees) revealed by multi-method thermochronology. *Comptes Rendus Géoscience*, *348*(3–4), 246–256. <https://doi.org/10.1016/j.crte.2016.01.001>
- Brun, J. P., & Fort, X. (2011). Salt tectonics at passive margins: Geology versus models. *Marine and Petroleum Geology*, *28*(6), 1123–1145. <https://doi.org/10.1016/j.marpetgeo.2011.03.004>
- Brune, S., Heine, C., Pérez-Gussinyé, M., & Sobolev, S. V. (2014). Rift migration explains continental margin asymmetry and crustal hyper-extension. *Nature Communications*, *5*, 4014. <https://doi.org/10.1038/ncomms5014>
- Butler, R. W., Tavarnelli, E., & Grasso, M. (2006). Structural inheritance in mountain belts: An Alpine–Apennine perspective. *Journal of Structural Geology*, *28*(11), 1893–1908. <https://doi.org/10.1016/j.jsg.2006.09.006>
- Butler, R. W. H. (1989). The influence of pre-existing basin structure on thrust system evolution in the Western Alps. *Geological Society, London, Special Publications*, *44*(1), 105–122. <https://doi.org/10.1144/gsl.sp.1989.044.01.07>
- Callot, J. P., Jahani, S., & Letouzey, J. (2007). The role of pre-existing diapirs in fold and thrust belt development. In *Thrust belts and foreland basins*, (pp. 309–325). Berlin, Heidelberg: Springer.
- Callot, J. P., Trocmé, V., Letouzey, J., Albouy, E., Jahani, S., & Sherkati, S. (2012). Pre-existing salt structures and the folding of the Zagros Mountains. *Geological Society, London, Special Publications*, *363*(1), 545–561. <https://doi.org/10.1144/sp363.27>
- Calvin, P., Casas-Sainz, A. M., Villalain, J. J., & Moussaid, B. (2018). Extensional vs. compressional deformation in the central high atlas salt province: A paleomagnetic approach. *Tectonophysics*, *734*, 130–147. <https://doi.org/10.1016/j.tecto.2018.04.007>
- Canérot, J. (1989). Rifting éocréacé et halocinèse sur la marge ibérique des Pyrénées occidentales (France). Conséquences structurales. *Bulletin des Centres de Recherches Exploration - Production Elf-Aquitaine*, *13*(1), 87–99. ISSN 0396-2687.
- Canérot, J. (2008). *Les Pyrénées: Histoire Géologique et Itinéraires de Découvertes* (p. 643). Pau, France: Atlantica-BRGM.

- Canérot, J., Hudec, M. R., & Rockenbauch, K. (2005). Mesozoic diapirism in the Pyrenean orogen: Salt tectonics on a transform plate boundary. *AAPG Bulletin*, 89(2), 211–229. <https://doi.org/10.1306/09170404007>
- Canérot, J., & Lenoble, J. L. (1993). Diapirisme cretace sur la marge iberique des Pyrenees occidentales; exemple du pic de Lauriolle; comparaisons avec l'Aquitaine, les Pyrenees centrales et orientales. *Bulletin de la Société Géologique de France*, 164(5), 719–726. ISSN: 0037-9409.
- Canérot, J., Peybernès, B., & Ciszak, R. (1978). Présence d'une marge méridionale à l'emplacement de la zone des Chainons béarnais (Pyrénées basco-béarnaises). *Bulletin de la société Géologique de France*, 7(5), 673–676. <https://doi.org/10.2113/gssgfbull.s7-xx.5.673>
- Casteras, M., Canérot, J., Paris, J. P., Tisin, D., Azambre, B., & Alimen, H. (1970). *Carte géol. France (1/50 000), feuille Oloron-Sainte-Marie (1051)*. Orléans, France: BRGM.
- Casteras, M., Villanova, M., & Godechot, Y. (1970). *Carte Géologique détaillée de la France, 1:50 000, feuille Lourdes (1052)*. Orléans: Bureau de Recherches Géologiques et Minières.
- Chadima, M., & Hrouda, F. (2006). Remasoft 3.0 a user-friendly paleomagnetic data browser and analyser. *Travaux Géophysiques*, 27, 20–21.
- Chelalou, R., Nalpas, T., Bousquet, R., Prevost, M., Lahfid, A., Poujol, M., et al. (2016). New sedimentological, structural and paleo-thermicity data in the Boucheville Basin (eastern north Pyrenean zone, France). *Comptes Rendus Géoscience*, 348(3–4), 312–321. <https://doi.org/10.1016/j.crte.2015.11.008>
- Clerc, C. (2012). *Evolution du domaine nord-pyrénéen au Crétacé: amincissement crustal extrême et thermicité élevée: un analogue pour les marges passives (Doctoral dissertation, Paris 6)*. Paris, France.
- Clerc, C., & Lagabrielle, Y. (2014). Thermal control on the modes of crustal thinning leading to mantle exhumation: Insights from the cretaceous Pyrenean hot paleomargins. *Tectonics*, 33, 1340–1359. <https://doi.org/10.1002/2013TC003471>
- Clerc, C., Lagabrielle, Y., Neumaier, M., Reynaud, J. Y., & De Saint-Blanquat, M. (2012). Exhumation of subcontinental mantle rocks: Evidence from ultramafic-bearing clastic deposits nearby the Lherz peridotite body, French Pyrenees. *Bulletin de la Société géologique de France*, 183(5), 443–459. <https://doi.org/10.2113/gssgfbull.183.5.443>
- Clerc, C., Lahfid, A., Monié, P., Lagabrielle, Y., Chopin, C., Poujol, M., et al. (2015). High-temperature metamorphism during extreme thinning of the continental crust: A reappraisal of the north Pyrenean passive paleomargin. *Solid Earth*, 6, 643–668. <https://doi.org/10.5194/se-6-643-2015>
- Cochelin, B. (2016). *Champ de déformation du socle paléozoïque des Pyrénées. Sciences de la Terre. Université Toulouse 3 Paul Sabatier (Doctoral dissertation)*. Retrieved from <https://tel.archives-ouvertes.fr/tel-01467202/document>
- Corre, B. (2017). *La bordure nord de la plaque ibérique à l'Albo-Cénomarien: architecture d'une marge passive de type ductile (Chainons Béarnais, Pyrénées Occidentales). (Doctoral dissertation, Rennes 1)*. Retrieved from <https://ged.univ-rennes1.fr/nuxeo/site/esupversions/7003bf82-b514-4ee8-a94a-374fa041ed6d?inline>
- Corre, B., Boulvais, P., Boiron, M. C., Lagabrielle, Y., Marasi, L., & Clerc, C. (2018). Fluid circulations in response to mantle exhumation at the passive margin setting in the North Pyrenean Zone France. *Mineralogy and Petrology*, 112(5), 647–670. <https://doi.org/10.1007/s00710-018-0559-x>
- Costa, E., & Vendeville, B. C. (2002). Experimental insights on the geometry and kinematics of fold-and-thrust belts above weak, viscous evaporitic décollement. *Journal of Structural Geology*, 24(11), 1729–1739. [https://doi.org/10.1016/s0191-8141\(01\)00169-9](https://doi.org/10.1016/s0191-8141(01)00169-9)
- Coward, M. P. (1983). Thrust tectonics, thin skinned or thick skinned, and the continuation of thrusts to deep in the crust. *Journal of Structural Geology*, 5(2), 113–123. [https://doi.org/10.1016/0191-8141\(83\)90037-8](https://doi.org/10.1016/0191-8141(83)90037-8)
- Crouzet, C., Ménard, G., & Rochette, P. (2001). Cooling history of the Dauphinoise zone (Western Alps, France) deduced from the thermopaleomagnetic record: Geodynamic implications. *Tectonophysics*, 340(1–2), 79–93. [https://doi.org/10.1016/s0040-1951\(01\)00142-1](https://doi.org/10.1016/s0040-1951(01)00142-1)
- Crouzet, C., Stang, H., Appel, E., Schill, E., & Gautam, P. (2001). Detailed analysis of successive pTRMs carried by pyrrhotite in Himalayan metacarbonates: An example from Hidden Valley, Central Nepal. *Geophysical Journal International*, 146(3), 607–618. <https://doi.org/10.1046/j.0956-540x.2001.01478.x>
- Davis, D. M., & Engelder, T. (1985). The role of salt in fold-and-thrust belts. *Tectonophysics*, 119(1–4), 67–88. [https://doi.org/10.1016/0040-1951\(85\)90033-2](https://doi.org/10.1016/0040-1951(85)90033-2)
- Debon, F. (1996). Pluton des Eaux-Chaudes In: Magmatisme hercynien. In A. Barnolas & J. C. Chiron (Eds.), *Synthèse géologique et géophysique des Pyrénées* (Vol. 1, p. 410). Orléans-Madrid: BRGM-ITGE.
- Debroas, E. J. (1987). Modèle de bassin triangulaire à l'intersection de décrochements divergents pour le fossé albo-cénomarien de la Ballongue (zone nord-pyrénéenne, France). *Bulletin de la Société géologique de France*, 3(5), 887–898. <https://doi.org/10.2113/gssgfbull.iii.5.887>
- Debroas, E. J. (1990). Le flysch noir albo-cénomarien témoin de la structuration alpine à sénonienne de la Zone nord-pyrénéenne en Bigorre (Hautes-Pyrénées, France). *Bulletin de la Société géologique de France*, 6(2), 273–285. <https://doi.org/10.2113/gssgfbull.vi.2.273>
- Dekkers, M. J., Mattéi, J. L., Fillion, G., & Rochette, P. (1989). Grain-size dependence of the magnetic behavior of pyrrhotite during its low-temperature transition at 34 K. *Geophysical Research Letters*, 16(8), 855–858. <https://doi.org/10.1029/GL016i008p00855>
- Ducoux, M. (2017). *Structure, thermicité et évolution géodynamique de la Zone Interne Métamorphique des Pyrénées. Sciences de la Terre. Université d'Orléans*. Retrieved from <https://hal.inria.fr/tel-01887025/>
- Ducoux, M., Jolivet, L., Callot, J. P., Aubourg, C., Masini, E., Lahfid, A., et al. (2019). The Nappe des Marbres unit of the Basque-Cantabrian Basin: The tectono-thermal evolution of a fossil hyperextended rift basin. *Tectonics*, 38, 3881–3915. <https://doi.org/10.1029/2018TC005348>
- Dumont, T., Replumaz, A., Rouméjon, S., Briais, A., Rigo, A., & Bouillin, J. P. (2015). Microseismicity of the Béarn range: Reactivation of inversion and collision structures at the northern edge of the Iberian plate. *Tectonics*, 34, 934–950. <https://doi.org/10.1002/2014TC003816>
- Duret, T., Petri, B., Mohn, G., Schmalholz, S. M., Schenker, F. L., & Müntener, O. (2016). The importance of structural softening for the evolution and architecture of passive margins. *Scientific Reports*, 6, 38,704. <https://doi.org/10.1038/srep38704>
- Escosa, F. O., Roca, E., & Ferrer, O. (2018). Testing thin-skinned inversion of a prerift salt-bearing passive margin (eastern Prebetic zone, SE Iberia). *Journal of Structural Geology*, 109, 55–73. <https://doi.org/10.1016/j.jsg.2018.01.004>
- Espurt, N., Angrand, P., Teixell, A., Labaume, P., Ford, M., de Saint Blanquat, M., & Chevrot, S. (2019). Crustal-scale balanced cross-section and restorations of the central Pyrenean belt (Nestes-Cinca transect): Highlighting the structural control of Variscan belt and Permian-Mesozoic rift systems on mountain building. *Tectonophysics*, 764, 25–45. <https://doi.org/10.1016/j.tecto.2019.04.026>
- Ferrer, O., Jackson, M. P. A., Roca, E., & Rubinat, M. (2012). Evolution of salt structures during extension and inversion of the offshore Parentis Basin (eastern Bay of Biscay). *Geological Society, London, Special Publications*, 363(1), 361–380. <https://doi.org/10.1144/sp363.16>
- Ferrer, O., Roca, E., Benjumea, B., Muñoz, J. A., Ellouz, N., & Team, M. (2008). The deep seismic reflection MARCONI-3 profile: Role of extensional Mesozoic structure during the Pyrenean contractional deformation at the eastern part of the Bay of Biscay. *Marine and Petroleum Geology*, 25(8), 714–730. <https://doi.org/10.1016/j.marpetgeo.2008.06.002>

- Fisher, R. A. (1953). Dispersion on a sphere. *Proceedings of the Royal Society of London A: Mathematical, Physical and Engineering Sciences*, 217(1130), 295–305. <https://doi.org/10.1098/rspa.1953.0064>
- Ford, M., Hemmer, L., Vacherat, A., Gallagher, K., & Christophoul, F. (2016). Retro-wedge foreland basin evolution along the ECORS line, eastern Pyrenees, France. *Journal of the Geological Society*, 173(3), 419–437. <https://doi.org/10.1144/jgs2015-129>
- Fortané, A., Duée, G., Lagabrielle, Y., & Coutelle, A. (1986). Lherzolites and the western “Chainons béarnais” (French Pyrenees): Structural and paleogeographical pattern. *Tectonophysics*, 129(1–4), 81–98. [https://doi.org/10.1016/0040-1951\(86\)90247-7](https://doi.org/10.1016/0040-1951(86)90247-7)
- Fuller, M. D. (1963). Magnetic anisotropy and paleomagnetism. *Journal of Geophysical Research*, 68(1), 293–309. <https://doi.org/10.1029/JZ068i001p00293>
- García-Sansegundo, J., Poblet, J., Alonso, J. L., & Clariana, P. (2011). Hinterland-foreland zonation of the Variscan orogen in the Central Pyrenees: Comparison with the northern part of the Iberian Variscan massif. *Geological Society, London, Special Publications*, 349(1), 169–184. <https://doi.org/10.1144/sp349.9>
- Gillett, S. L. (2003). Paleomagnetism of the notch peak contact metamorphic aureole, revisited: Pyrrhotite from magnetite + pyrite under submetamorphic conditions. *Journal of Geophysical Research*, 108(B9), 2446. <https://doi.org/10.1029/2002JB002386>
- Golberg, J. M., & Leyrelop, A. F. (1990). High temperature-low pressure cretaceous metamorphism related to crustal thinning (eastern north Pyrenean zone, France). *Contributions to Mineralogy and Petrology*, 104(2), 194–207. <https://doi.org/10.1007/bf00306443>
- Golberg, J. M., & Maluski, H. (1988). Données nouvelles et mise au point sur l'âge du métamorphisme pyrénéen. *Comptes rendus de l'Académie des sciences. Série 2, Mécanique, Physique, Chimie, Sciences de l'univers, Sciences de la Terre*, 306(6), 429–435. ISSN 0764-4450.
- Gómez-Paccard, M., López-Blanco, M., Costa, E., Garcés, M., Beamud, E., & Larrasoña, J. C. (2012). Tectonic and climatic controls on the sequential arrangement of an alluvial fan/fan-delta complex (Montserrat, Eocene, Ebro Basin, NE Spain). *Basin Research*, 24(4), 437–455. <https://doi.org/10.1111/j.1365-2117.2011.00532.x>
- Gómez-Romeu, J., Masini, E., Tugend, J., Ducoux, M., & Kuszniir, N. (2019). Role of rift structural inheritance in orogeny highlighted by the Western Pyrenees case-study. *Tectonophysics*, 766, 131–150. <https://doi.org/10.1016/j.tecto.2019.05.022>
- Gradstein, F. M., Ogg, J. G., Schmitz, M., & Ogg, G. (Eds.) (2012). *The geologic time scale 2012*. Netherlands: Elsevier.
- Graham, R., Jackson, M. P. A., Pilcher, R., & Kilsdonk, B. (2012). Allochthonous salt in the sub-Alpine fold-thrust belt of haute Provence, France. *Geological Society of London, Special Publication*, 363, 595–615. <https://doi.org/10.1144/SP363.30>
- Granado, P., Roca, E., Strauss, P., Pelz, K., & Muñoz, J. A. (2018). Structural styles in fold-and-thrust belts involving early salt structures: The northern calcareous Alps (Austria). *Geology*, 47(1), 51–54. <https://doi.org/10.1130/g45281.1>
- Grunnalaite, I., & Mosbron, A. (2019). On the significance of salt modelling—Example from modelling of salt tectonics, temperature and maturity around salt structures in southern North Sea. *Geosciences*, 9(9), 363. <https://doi.org/10.3390/geosciences9090363>
- Guenther, W. R., Reiners, P. W., Ketcham, R. A., Nasdala, L., & Giester, G. (2013). Helium diffusion in natural zircon: Radiation damage, anisotropy, and the interpretation of zircon (U-Th)/he thermochronology. *American Journal of Science*, 313(3), 145–198. <https://doi.org/10.2475/03.2013.01>
- Hart, N. R., Stockli, D. F., Lavier, L. L., & Hayman, N. W. (2017). Thermal evolution of a hyperextended rift basin, Mauléon Basin, western Pyrenees. *Tectonics*, 36, 1103–1128. <https://doi.org/10.1002/2016TC004365>
- Izquierdo-Llavall, E., Roca, E., Xie, H., Pla, O., Muñoz, J. A., Rowan, M. G., et al. (2018). Influence of overlapping décollements, Syntectonic sedimentation, and structural inheritance in the evolution of a Contractional system: The central Kuqa fold-and-thrust belt (Tian Shan Mountains, NW China). *Tectonics*, 37, 2608–2632. <https://doi.org/10.1029/2017TC004928>
- Izquierdo-Llavall, E., Román-Berdiel, T., Casas, A. M., Oliva-Urcia, B., Gil-Pena, I., Soto, R., & Jabaloy, A. (2012). Magnetic and structural study of the Eaux-Chaudes intrusion: Understanding the Variscan deformation in the Western axial zone (Pyrenees). *International Journal of Earth Sciences*, 101(7), 1817–1834. <https://doi.org/10.1007/s00531-012-0760-9>
- Jahani, S., Callot, J. P., de Lamotte, D. F., Letouzey, J., & Leturmy, P. (2007). The salt diapirs of the Eastern Fars Province (Zagros, Iran): A brief outline of their past and present. In *Thrust belts and foreland basins*, (pp. 289–308). Berlin, Heidelberg: Springer.
- James, V., & Canérot, J. (1999). Diapirisme et structuration post-triasique des Pyrénées occidentales et de l'Aquitaine méridionale (France). *Eclogae Geologicae Helveticae*, 92(1), 63–72.
- Jammes, S., Lavier, L., & Manatschal, G. (2010). Extreme crustal thinning in the Bay of Biscay and the Western Pyrenees: From observations to modelling. *Geochemistry, Geophysics, Geosystems*, 11, Q10016. <https://doi.org/10.1029/2010GC003218>
- Jammes, S., Manatschal, G., Lavier, L., & Masini, E. (2009). Tectonosedimentary evolution related to extreme crustal thinning ahead of a propagating ocean: Example of the western Pyrenees. *Tectonics*, 28, TC4012. <https://doi.org/10.1029/2008TC002406>
- Jensen, P. K. (1983). Calculations on the thermal conditions around a salt diapir. *Geophysical Prospecting*, 31(3), 481–489. <https://doi.org/10.1111/j.1365-2478.1983.tb01064.x>
- Jourdon, A., Mouthereau, F., Le Pourhiet, L., & Callot, J. P. (2020). Topographic and tectonic evolution of mountain belts controlled by salt thickness and rift architecture. *Tectonics*, 39, e2019TC005719. <https://doi.org/10.1029/2019TC005903>
- Kaiser, B. O., Cacace, M., Scheck-Wenderoth, M., & Lewerenz, B. (2011). Characterization of main heat transport processes in the northeast German Basin: Constraints from 3-D numerical models. *Geochemistry, Geophysics, Geosystems*, 12, Q07011. <https://doi.org/10.1029/2011GC003535>
- Koymans, M. R., Langereis, C. G., Pastor-Galán, D., & van Hinsbergen, D. J. (2016). Paleomagnetism. Org: An online multi-platform open source environment for paleomagnetic data analysis. *Computers and Geosciences*, 93, 127–137. <https://doi.org/10.1016/j.cageo.2016.05.007>
- Labaupe, P., & Teixell, A. (2014). *Diapir rising and squeezing in the north-Pyrenean realm (Chainons Béarnais): From mid-cretaceous hyperextension to Pyrenean inversion*, (Vol. 230). Pau: Résumés de la 24e Réunion des sciences de la Terre.
- Lacan, P., Nivière, B., Rousset, D., & Sénéchal, P. (2012). Late Pleistocene folding above the mail Arrouy thrust, North-Western Pyrenees (France). *Tectonophysics*, 541, 57–68. <https://doi.org/10.1016/j.tecto.2012.03.022>
- Lagabrielle, Y., & Bodinier, J. L. (2008). Submarine reworking of exhumed subcontinental mantle rocks: Field evidence from the Lherz peridotites, French Pyrenees. *Terra Nova*, 20(1), 11–21. <https://doi.org/10.1111/j.1365-3121.2007.00781.x>
- Lagabrielle, Y., Labaupe, P., & de Saint Blanquat, M. (2010). Mantle exhumation, crustal denudation, and gravity tectonics during cretaceous rifting in the Pyrenean realm (SW Europe): Insights from the geological setting of the lherzolite bodies. *Tectonics*, 29(4). <https://doi.org/10.1029/2009TC002588>
- Lago, M., Arranz, E., Pocovi, A., Galé, C., & Gil-Imaz, A. (2004). Permian magmatism and basin dynamics in the southern Pyrenees: A record of the transition from late Variscan transtension to early Alpine extension. *Geological Society, London, Special Publications*, 223(1), 439–464. <https://doi.org/10.1144/gsl.sp.2004.223.01.19>
- Lahfid, A., Beyssac, O., Deville, E., Negro, F., Chopin, C., & Goffé, B. (2010). Evolution of the Raman spectrum of carbonaceous material in low-grade metasediments of the Glarus Alps (Switzerland). *Terra Nova*, 22(5), 354–360. <https://doi.org/10.1111/j.1365-3121.2010.00956.x>

- Lambert, J. M., Simkovich, G., & Walker, P. L. (1998). The kinetics and mechanism of the pyrite-to-pyrrhotite transformation. *Metallurgical and Materials Transactions B*, 29(2), 385–396. <https://doi.org/10.1007/s11663-998-0115-x>
- Legeay, E., Ringenbach, J. C., Kergaravat, C., Pichat, A., Mohn, G., Vergés, J., et al. (2019). Structure and kinematics of the Central Sivas Basin (Turkey): Salt deposition and tectonics in an evolving fold-and-thrust belt. *Geological Society, London, Special Publications*, 490, SP490–SP2019. <https://doi.org/10.1144/sp490-2019-92>
- Letouzey, J., Colletta, B., Vially, R., & Chermette, J. C. (1995). Evolution of salt-related structures in compressional settings. In M. P. A. Jackson, D. G. Roberts, & S. Snelson (Eds.), *Salt tectonics: A global perspective: AAPG Memoir* (Vol. 65, pp. 41–60). Tulsa, OK: AAPG.
- López-Mir, B., Muñoz, J. A., & García-Senz, J. (2015). Extensional salt tectonics in the partially inverted Cotiella post-rift basin (South-Central Pyrenees): Structure and evolution. *International Journal of Earth Sciences*, 104(2), 419–434. <https://doi.org/10.1007/s00531-014-1091-9>
- Lowrie, W. (1990). Identification of ferromagnetic minerals in a rock by coercivity and unblocking temperature properties. *Geophysical Research Letters*, 17(2), 159–162. <https://doi.org/10.1029/GL017i002p00159>
- Luján, M., Storti, F., Balanyá, J. C., Crespo-Blanc, A., & Rossetti, F. (2003). Role of décollement material with different rheological properties in the structure of the Aljibe thrust imbricate (Flysch trough, Gibraltar arc): An analogue modelling approach. *Journal of Structural Geology*, 25(6), 867–881. [https://doi.org/10.1016/s0191-8141\(02\)00087-1](https://doi.org/10.1016/s0191-8141(02)00087-1)
- Masini, E., Manatschal, G., Tugend, J., Mohn, G., & Flament, J. M. (2014). The tectono-sedimentary evolution of a hyper-extended rift basin: The example of the Arzacq–Mauléon rift system (Western Pyrenees, SW France). *International Journal of Earth Sciences*, 103(6), 1569–1596. <https://doi.org/10.1007/s00531-014-1023-8>
- Matte, P. (2002). Les plis hercyniens kilométriques couchés vers l'ouest-sud-ouest dans la région du pic du Midi d'Ossau–col du Somport (zone axiale des Pyrénées occidentales). *Comptes Rendus Geosciences*, 334, 773–779. [https://doi.org/10.1016/s1631-0713\(02\)01808-4](https://doi.org/10.1016/s1631-0713(02)01808-4)
- McClay, K., Dooley, T., & Zamora, G. (2003). Analogue models of delta systems above ductile substrates. *Geological Society, London, Special Publications*, 216(1), 411–428. <https://doi.org/10.1144/gsl.sp.1989.044.01.04>
- McClay, K., Muñoz, J. A., & García-Senz, J. (2004). Extensional salt tectonics in a contractional orogen: A newly identified tectonic event in the Spanish Pyrenees. *Geology*, 32(9), 737–740. <https://doi.org/10.1130/g20565.1>
- McClay, K. R. (1989). Analogue models of inversion tectonics. *Geological Society, London, Special Publications*, 44(1), 41–59. <https://doi.org/10.1144/gsl.sp.1989.044.01.04>
- Monod, B., Bourroullec, I., Chèvremont, P., LeBayon, B., Nehlig, P., Aretz, M., et al. (2014). *Carte géologique numérique à 1/250 000 de la région Midi-Pyrénées*. Notice Orléans, France: BRGM.
- Mouthereau, F., Filleaudeau, P.-Y., Vacherat, A., Pik, R., Lacombe, O., Fellin, M. G., et al. (2014). Placing limits to shortening evolution in the Pyrenees: Role of margin architecture and implications for the Iberia/Europe convergence. *Tectonics*, 33, 2283–2314. <https://doi.org/10.1002/2014TC003663>
- Muñoz, J. A. (1992). Evolution of a continental collision belt: ECORS-Pyrenees crustal balanced cross-section. In *Thrust tectonics*, (pp. 235–246). Dordrecht: Springer.
- Muñoz, J. A. (2002). The Pyrenees. In *The geology of Spain* (pp. 370–385). London, UK: Geological Society of London.
- Nirrengarten, M., Manatschal, G., Tugend, J., Kuszniir, N., & Sauter, D. (2018). Kinematic evolution of the southern North Atlantic: Implications for the formation of hyperextended rift systems. *Tectonics*, 37, 89–118. <https://doi.org/10.1002/2017TC004495>
- Oliva-Urcia, B., Casas, A. M., Pueyo, E. L., Román-Berdiel, T., & Geissman, J. W. (2010). Paleomagnetic evidence for dextral strike-slip motion in the Pyrenees during alpine convergence (Mauléon basin, France). *Tectonophysics*, 494(3–4), 165–179. <https://doi.org/10.1016/j.tecto.2010.09.018>
- Osete, M. L., & Palencia-Ortas, A. (2006). Polos Paleomagnéticos de Iberia de los últimos 300 millones de años. *Física de la Tierra*, 18, 157–181. ISSN: 0214-4557.
- Pedreira, A., García-Senz, J., Ayala, C., Ruiz-Constán, A., Rodríguez-Fernández, L. R., Robador, A., & González Menéndez, L. (2017). Reconstruction of the exhumed mantle across the north Iberian margin by crustal-scale 3-D gravity inversion and geological cross-section. *Tectonics*, 36, 3155–3177. <https://doi.org/10.1002/2017TC004716>
- Pla, O., Roca, E., Xie, H., Izquierdo-Llavall, E., Muñoz, J. A., Rowan, M. G., et al. (2019). Influence of Syntectonic sedimentation and Décollement rheology on the geometry and evolution of Orogenic wedges: Analog modeling of the Kuqa fold-and-Thrust Belt (NW China). *Tectonics*, 38, 2727–2755. <https://doi.org/10.1029/2018TC005386>
- Poidras, Th., Nicol, P., Camps, P. (2012). Patent # 1256194, June 28, 2012; Title: «Device for conditioning sample of e.g. rock to be analyzed e.g. to determine magnetic field at level of geological times, has application assembly generating magnetic field desired in volume, and control unit adjusting intensity of field» <https://app.dimensions.ai/details/patent/FR-2992731-A1>
- Poitevin, C., Labaume, P., Gay, A., & Teixell, A. (2014). *Du rifting à l'inversion pyrénéenne dans le Bassin d'Aquitaine: interprétation du profil sismique St-Pé de Bigorre-Condom*, (p. 327). Pau: Résumés de la 24e Réunion des Sciences de la Terre.
- Puigdefàbregas, C. (1975). La sedimentación molásica en la cuenca de Jaca. *Pirineos*, 104, 1–188.
- Roca, E., Muñoz, J. A., Ferrer, O., & Ellouz, N. (2011). The role of the Bay of Biscay Mesozoic extensional structure in the configuration of the Pyrenean orogen: Constraints from the MARCONI deep seismic reflection survey. *Tectonics*, 30, TC2001. <https://doi.org/10.1029/2010TC002735>
- Rochette, P. (1988). Inverse magnetic fabric in carbonate-bearing rocks. *Earth and Planetary Science Letters*, 90(2), 229–237. [https://doi.org/10.1016/0012-821x\(88\)90103-3](https://doi.org/10.1016/0012-821x(88)90103-3)
- Rochette, P., Fillion, G., Mattéi, J. L., & Dekkers, M. J. (1990). Magnetic transition at 30–34 kelvin in pyrrhotite: Insight into a widespread occurrence of this mineral in rocks. *Earth and Planetary Science Letters*, 98(3–4), 319–328. [https://doi.org/10.1016/0012-821x\(90\)90034-u](https://doi.org/10.1016/0012-821x(90)90034-u)
- Rosenbaum, G., Lister, G. S., & Duboz, C. (2002). Relative motions of Africa, Iberia and Europe during Alpine orogeny. *Tectonophysics*, 359(1–2), 117–129. [https://doi.org/10.1016/s0040-1951\(02\)00442-0](https://doi.org/10.1016/s0040-1951(02)00442-0)
- Rouvier, H., Henry, B., & Le Goff, M. (2012). Mise en évidence par le paléomagnétisme de rotations régionales dans la virgation des Corbières (France). *Bulletin de la Société géologique de France*, 183(5), 409–424. <https://doi.org/10.2113/gssgfbull.183.5.409>
- Rowan, M. G., Peel, F. J., & Vendeville, B. C. (2004). Gravity-driven fold belts on passive margins. In K. R. McClay (Ed.), *Thrust tectonics and hydrocarbon systems: AAPG memoir* (Vol. 82, pp. 157–182). Tulsa, OK: AAPG.
- Santolaria, P., Vendeville, B. C., Graveleau, F., Soto, R., & Casas-Sainz, A. (2015). Double evaporitic décollements: Influence of pinch-out overlapping in experimental thrust wedges. *Journal of Structural Geology*, 76, 35–51. <https://doi.org/10.1016/j.jsg.2015.04.002>
- Saura, E., Ardèvol i Oró, L., Teixell, A., & Vergés, J. (2016). Rising and falling diapirs, shifting depocenters, and flap overturning in the cretaceous Sopeira and Sant Gervàs subbasins (Ribagorça Basin, southern Pyrenees). *Tectonics*, 35, 638–662. <https://doi.org/10.1002/2015TC004001>
- Saura, E., & Teixell, A. (2006). Inversion of small basins: Effects on structural variations at the leading edge of the axial zone antiformal stack (southern Pyrenees, Spain). *Journal of Structural Geology*, 28(11), 1909–1920. <https://doi.org/10.1016/j.jsg.2006.06.005>

- Schettino, A., & Turco, E. (2011). Tectonic history of the western Tethys since the late Triassic. *Bulletin*, 123(1–2), 89–105. <https://doi.org/10.1130/b30064.1>
- Schill, E., Appel, E., Crouzet, C., Gautam, P., Wehland, F., & Staiger, M. (2004). Oroclinal bending versus regional significant clockwise rotations in the Himalayan arc—Constraints from secondary pyrrhotite remanences. *Orogenic Curvature: Integrating Paleomagnetic and Structural Analyses*, 383, 73. [https://doi.org/10.1130/0-8137-2383-3\(2004\)383\[73:obvrsc\]2.0.co;2](https://doi.org/10.1130/0-8137-2383-3(2004)383[73:obvrsc]2.0.co;2)
- Serrano, O., Delmas, J., Hanot, F., Vially, R., Herbon, J. P., Houel, P., & Tourlière, B. (2006). *Le Bassin d'Aquitaine: valorisation de données sismiques, cartographie structurale et potentiel pétrolier*, Ed. Orléans: BRGM.
- Soula, J. C., Debat, P., Deramond, J., & Pouget, P. (1986). A dynamic model of the structural evolution of the Hercynian Pyrenees. *Tectonophysics*, 129(1–4), 29–51. [https://doi.org/10.1016/0040-1951\(86\)90244-1](https://doi.org/10.1016/0040-1951(86)90244-1)
- Souquet, P., Debrosses, E. J., Boirie, J. M., Pons, P., Fixari, G., Roux, J. C., et al. (1985). *The black flysh group (albian-Cenomanian) of the Pyrenees* (Vol. 9, pp. 183–252). Pau, France: Bull Cent Rech Explor Prod Elf-aquitaine.
- Speksnijder, A. (1985). Anatomy of a strike-slip fault controlled sedimentary basin, Permian of the southern Pyrenees, Spain. *Sedimentary Geology*, 44(3–4), 179–223. [https://doi.org/10.1016/0037-0738\(85\)90014-4](https://doi.org/10.1016/0037-0738(85)90014-4)
- Taberner, C., Dinarès-Turell, J., Giménez, J., & Docherty, C. (1999). Basin infill architecture and evolution from magnetostratigraphic cross-basin correlations in the southeastern Pyrenean foreland basin. *Geological Society of America Bulletin*, 111(8), 1155–1174. [https://doi.org/10.1130/0016-7606\(1999\)111<1155:biaaf>2.3.co;2](https://doi.org/10.1130/0016-7606(1999)111<1155:biaaf>2.3.co;2)
- Tauxe, L., & Watson, G. S. (1994). The fold test: An eigen analysis approach. *Earth and Planetary Science Letters*, 122(3–4), 331–341. [https://doi.org/10.1016/0012-821x\(94\)90006-x](https://doi.org/10.1016/0012-821x(94)90006-x)
- Teixell, A. (1996). The Ansó transect of the southern Pyrenees: Basement and cover thrust geometries. *Journal of the Geological Society*, 153(2), 301–310. <https://doi.org/10.1144/gsjgs.153.2.0301>
- Teixell, A. (1998). Crustal structure and orogenic material budget in the west Central Pyrenees. *Tectonics*, 17(3), 395–406. <https://doi.org/10.1029/98tc00561>
- Teixell, A., Labaume, P., & Lagabrielle, Y. (2016). The crustal evolution of the west-Central Pyrenees revisited: Inferences from a new kinematic scenario. *Comptes Rendus Geoscience*, 348(3–4), 257–267. <https://doi.org/10.1016/j.crte.2015.10.010>
- Ternet, Y., Barrère, P., Bois, J. P., Debon, F., Godechot, Y., Mirouse, R., et al. (1980). *Geological map of Argelès-Gazost (1/50 000)*. Orléans, France: BRGM.
- Ternet, Y., Barrère, P., & Canérot, J. (2004). *Geological map of Laruns-Somport (1/50 000)*. Orléans, France: BRGM.
- Torres-López, S., Casas, A. M., Villalain, J. J., Moussaid, B., Ruiz Martínez, V. C., & El-Ouardi, H. (2018). Evolution of the ridges of Midelt-Errachidia section in the high atlas revealed by paleomagnetic data. *Tectonics*, 37, 3018–3040. <https://doi.org/10.1029/2017TC004936>
- Tugend, J., Manatschal, G., & Kuszniir, N. J. (2015). Spatial and temporal evolution of hyperextended rift systems: Implication for the nature, kinematics, and timing of the Iberian-European plate boundary. *Geology*, 43(1), 15–18. <https://doi.org/10.1130/g36072.1>
- Tugend, J., Manatschal, G., Kuszniir, N. J., Masini, E., Mohn, G., & Thion, I. (2014). Formation and deformation of hyperextended rift systems: Insights from rift domain mapping in the Bay of Biscay-Pyrenees. *Tectonics*, 33, 1239–1276. <https://doi.org/10.1002/2014TC003529>
- Vacherat, A., Mouthereau, F., Pik, R., Bernet, M., Gautheron, C., Masini, E., et al. (2014). Thermal imprint of rift-related processes in orogens as recorded in the Pyrenees. *Earth and Planetary Science Letters*, 408, 296–306. <https://doi.org/10.1016/j.epsl.2014.10.014>
- Vendeville, B. C., Ge, H., & Jackson, M. P. A. (1995). Scale models of salt tectonics during basement-involved extension. *Petroleum Geoscience*, 1(2), 179–183. <https://doi.org/10.1144/petgeo.1.2.179>
- Wang, Y., Chevrot, S., Monteiller, V., Komatitsch, D., Mouthereau, F., Manatschal, G., et al. (2016). The deep roots of the western Pyrenees revealed by full waveform inversion of teleseismic P waves. *Geology*, 44(6), 475–478. <https://doi.org/10.1130/g37812.1>
- Wehland, F., Eibl, O., Kotthoff, S., Alt-Epping, U., & Appel, E. (2005). Pyrrhotite pTRM acquisition in metamorphic limestones in the light of microscopic observations. *Physics of the Earth and Planetary Interiors*, 151(1–2), 107–114. <https://doi.org/10.1016/j.pepi.2005.01.005>
- Zwart, H. J. (1986). The Variscan geology of the Pyrenees. *Tectonophysics*, 129(1–4), 9–27. [https://doi.org/10.1016/0040-1951\(86\)90243-x](https://doi.org/10.1016/0040-1951(86)90243-x)